eprints@whiterose.ac.uk
https://eprints.whiterose.ac.uk/

Progressive ductile shearing during till accretion within the deforming bed of a palaeo-ice stream

Emrys Phillips [1]*, Matteo Spagnolo [2], Alasdair C.J. Pilmer [2], Brice R. Rea [2], Jan A. Piotrowski [3], Jeremy C. Ely[4] and Simon Carr [5]

1 British Geological Survey, The Lyell Centre, Research Avenue South, Edinburgh EH14 4AP, UK

2 Department of Geography and the Environment, School of Geosciences, University of Aberdeen, Aberdeen AB24 3UF, UK

3 Department of Geoscience, Aarhus University, Denmark

4 Department of Geography, University of Sheffield, Sheffield S10 2TN, UK

5 School of Geography, Queen Mary, University of London, Mile End Road, London E1 4NS, UK

* Corresponding author: e-mail - erp@bgs.ac.uk

Abstract

This paper presents the results of a detailed microstructural study of a thick till formed beneath the Weichselian (Devensian) Odra palaeo-ice stream, west of Środa Wielkopolska, Poland. This SE-flowing ice stream was one of a number of corridors of faster flowing ice which drained the Scandinavian Ice Sheet in the Baltic region. Macroscopically, the massive, laterally extensive till which formed the bed of this ice stream lacks any obvious evidence of glaciotectonism (thrusting, folding). However, microscale analysis reveals that bed deformation was dominated by foliation development, recording progressive ductile shearing within a subhorizontal subglacial shear zone. Five successive generations of clast microfabric (S1 to S5) have been identified defining a set of up-ice and down-ice dipping Riedel shears, as well as a subhorizontal shear foliation coplanar to the ice-bed interface. Cross-cutting relationships between the shear fabrics record temporal changes in the style of deformation during this progressive shear event. Kinematic indicators (S-C and ECC-type fabrics) within the till indicate a consistent SE-directed shear sense, in agreement with the regional ice flow pattern. A model of bed deformation involving incremental progressive simple shear during till accretion is proposed. The relative age of this deformation was diachronous becoming progressively younger upwards, compatible with subglacial shearing having accompanied till accretion at the top of the deforming bed. Variation in the relative intensity of the microfabrics

31 records changes in the magnitude of the cumulative strain imposed on the till and the degree of
32 coupling between the ice and underlying bed during fast ice flow.

33 # 1. Introduction

34 Ice streams play an important role in regulating the behaviour of modern ice sheets (e.g. Antarctica,

35 Bamber *et al.*, 2000) and take the form of corridors of fast flowing ice bounded by ice flowing up to

36 an order of magnitude slower (Stokes and Clark, 2001; Bennett, 2003). However the factors

37 controlling fast ice flow are incompletely understood. Published studies of modern and ancient ice

38 stream beds have led to two possible explanations governing ice stream flow: (i) basal sliding

39 facilitated by elevated water pressures at the ice-bed interface with the ice stream effectively

40 becoming decoupled from the underlying sediments (e.g. Alley, 1989; Piotrowski and Tulaczyk, 1999)

41 or hard bedrock substrate (Margold *et al.*, 2015); and (ii) basal motion accommodated by

42 deformation of either a thick (several metres) or thin (centimetres to decimetres) layer of 'soft'

43 sediments (till) (e.g. Alley *et al.*, 1986, 1987a, b; Boulton and Hindmarsh, 1987; Clarke, 1987;

44 Humphrey *et al.*, 1993; Boulton *et al.*, 2001). However, in reality these two processes are not

45 mutually exclusive and may periodically "switch" to form the dominant movement mechanism of ice

46 stream movement depending upon the water content and/or pressure within the bed.

47 Understanding these processes has fundamental implications for our understanding of subglacial

48 sediment erosion, transport and deposition. Furthermore a greater understanding of the subglacial

49 environment of ice streams may also elucidate controls on ice streaming such as basal thermal

50 regime (Hindmarsh, 2009) and/or subglacial hydrology (Kyrke-Smith *et al.*, 2015), leading to the

51 development of more sophisticated and robust models of ice stream flow dynamics and, ultimately,

52 ice sheet mass balance and sea-level change.

53 The recognition of a characteristic suite of subglacial landforms (including megascale glacial

54 lineations) formed beneath palaeo-ice streams (e.g. Dyke and Morris, 1988; Hodgson, 1994;

55 Patterson, 1997, 1998; Clark and Stokes, 2001, 2002, 2003) has enabled the establishment of a set of

56 criteria for identifying the presence and areal extent of these ancient ice streams (Stokes and Clark,

57 1999). These criteria have been, at least partially, validated by observations of the subglacial

58 landscape beneath contemporary Antarctic ice-streams (King *et al.*, 2009; Bingham *et al.*, 2017). The

59 exposed beds of palaeo-ice streams provide an ideal laboratory to investigate the sedimentary and

60 structural processes occurring beneath fast flowing ice. However, on a macroscale the sediments

61 (tills) deposited beneath many palaeo-ice streams are massive, lacking any visible signs of

62 stratification and/or glacitectonic deformation (see Evans, 2018 and references therein). As a

63 consequence micromorphology is increasingly being used as a primary tool for the analysis of these

and other subglacial sediments (tills) (see Menzies and Maltman, 1992; van der Meer, 1979, 1987; Menzies *et al.*, 1997; Khatwa and Tulaczyk, 2001; van der Meer *et al.*, 2003; Hiemstra *et al.*, 2005; Baroni and Fasano, 2006; Larsen *et al.*, 2006, 2007; Phillips *et al.*, 2007, 2011, 2013, 2018; Narloch *et al.*, 2012; Neudorf *et al.*, 2013; Gehrmann *et al.*, 2017; Evans, 2018). This technique can provide far greater detail on the depositional and deformation histories recorded by these sediments than can be obtained from macroscale studies alone; for example, unravelling the often complex deformation histories recorded by glacigenic sequences (van der Meer, 1993; Phillips and Auton, 2000; van der Wateren *et al.*, 2000; Menzies, 2000; Phillips *et al.*, 2007; Lee and Phillips, 2008; Vaughan-Hirsch *et al.*, 2013; Narloch *et al.*, 2012, 2013) and the role played by pressurised meltwater during their deformation (Hiemstra and van der Meer, 1997; Phillips and Merritt, 2008; van der Meer *et al.*, 2009; Denis *et al.*, 2010; Phillips *et al.*, 2013; 2018; Narloch *et al.*, 2012, 2013).

This paper presents the results of a detailed micromorphological study of the thick till sequence laid down by the Weichselian (Devensian) Odra palaeo-ice stream as it flowed SE across Wielkopolska Lowlands of Poland (Fig. 1). The study area is located near Poznań, in a region dominated by NW-SE-trending subglacial landforms (megascale lineations) interpreted as having been formed during fast ice flow (Przybylski, 2008; Spagnolo *et al.*, 2016). Thin sections are used to investigate the strain signature imparted by this palaeo-ice stream on the laterally extensive till formed within its bed. The results of this detailed microstructural study have been used to investigate the nature of deformation and in particular foliation development during progressive ductile simple shear within an evolving subhorizontal subglacial shear zone. Spatial variations in the relative intensity of the microfabrics are interpreted as recording changes in the magnitude of the cumulative strain imposed on the till, potentially reflecting the degree of ice-bed coupling during fast ice flow.

2. Location of study area and geological setting

During the Weichselian (Devensian) glaciation much of the Baltic region was covered by the Scandinavian Ice Sheet. This ice sheet was drained by a series of ice streams, including the Odra palaeo-ice stream (OPIS) which flowed SE across the Wielkopolska Lowland region of western Poland (Przybylski, 2008; Spagnolo *et al.*, 2016). In this region, the bed of the Odra palaeo-ice stream (over 1000 km^2) is characterised by a suite of well-preserved NW-SE-trending megascale glacial lineations (MSGL) underlain by a thick (c. 30 m) sequence of Quaternary sediments. This study is focused on the bed of the OPIS to the west of the town of Środa Wielkopolska, approximately 30 km southeast of Poznań (Fig. 1a, b), close to the c. 21 ka Leszno phase ice margin (Kozarski, 1988; Przybylski, 2008; Marks, 2012). The geomorphology of the study area (c. 180 km^2) is dominated by a suite of elongate

3

97   (>16 km long), low-relief (2-4 m high) MSGL with a crest-to-crest spacing of 600-800 m (Fig. 1c). It is

98   possible that these landforms were originally much longer (Przybylski, 2008) as they have been

99   locally truncated by glacifluvial erosion, as well as the extensive urbanisation of the region which has

100 locally overprinted/strongly modified this subglacial landscape. Although locally modified the

101 morphology of these subglacial landforms are comparable to MSGL described from other palaeo-ice

102 stream settings worldwide (Spagnolo *et al*., 2014).

103 The sediments making up the bed of the OPIS are in general poorly exposed and detailed

104 sedimentological analysis of these deposits has relied upon trenches excavated at key positions

105 across the MSGL's (Fig. 1c; see below). The trenches reveal that these subglacial landforms are

106 composed of a homogeneous, matrix-supported, yellow coloured silty-sandy diamicton (Fig. 1d)

107 containing rare gravel (2-64 mm) and extremely rare cobble (>64 mm) sized clasts (Spagnolo *et al*.,

108 2016). The massive, laterally extensive diamicton (interpreted as a subglacial traction till; sensu

109 Evans *et al*., 2006) lacks any obvious macroscale evidence of glaciotectonism (e.g. thrusting, folding…

110 etc.) and no other sedimentary units have been recognised. Fine gravel clasts (2-4 mm) contained

111 within the diamicton are composed of a range of sedimentary and crystalline rock fragments,

112 including Palaeozoic limestones derived from the Baltic Basin as well as metamorphic and igneous

113 rocks from Scandinavia, indicating that this deposit contains a significant far-travelled component

114 (Spagnolo *et al*., 2016). The diamicton is relatively unaltered, exhibiting only very minor to rare

115 macroscopic evidence of calcification, typically occurring in patches of <200 cm^2. Clast a-axis

116 macrofabric data published by Spagnolo *et al*. (2016) are remarkably uniform (vertically and

117 laterally) across the bed of the OPIS within the study area. These shallow dipping macrofabrics are

118 orientated NW-SE, concordant with the long axes of the MSGL and parallel to the regional ice flow

119 direction.

120 # 3. Methods

121 Detailed analysis of the till forming the bed of the OPIS has focussed on 10 sites located on the crests

122 (A, B, C, D, E, K, T; Fig. 1c) and flanks (X, Y, Z; Fig. 1c) of three of the mega-scale lineations. A trench

123 (6-10 m long, 2-3 m wide and 3-5 m deep) was excavated at each site (Fig. 1d) and the samples for

124 thin section preparation collected using standard Kubiena tins. Prior to sampling, the temporarily

125 exposed sections were logged, photographed and described in detail with particular emphasis being

126 placed on recording the macroscale variation in lithology and structure of the till. The samples were

127 collected in a vertical profile (e.g. C1M highest to C6M lowest) below the base of the modern soil

128 and with a 20 cm spacing between each Kubiena tin (Fig. 1d). This approach was adopted to provide

129 detailed   information   on   the   range   of   microstructures   developed   at   different

4

130 stratigraphical/structural levels within the till. The Kubiena tins were either cut or pushed into the
131 face in order to limit sample disturbance. The position of the sample within the sequence, its
132 orientation relative to magnetic north, depth and way-up were marked on the outside of the tin
133 during collection.

134   Sample preparation was carried out at Royal Holloway, University of London, using the
135 methods outlined by Palmer (2005). Large format (10 x 8 cm), orientated (parallel to the long axis of
136 the MSGL and former ice flow direction) thin sections were taken from the centre of each of the
137 resin impregnated samples, avoiding artefacts associated with sample collection. The thin sections
138 were described using a Zeiss petrological microscope revealing that the composition, texture and
139 structure of the diamicton are uniform across the study area. The detailed microscale study focused
140 upon site C, located on the crest of a prominent NW-SE-trending MSGL, as well as three samples
141 from sites X, Y and Z, which provide a traverse across the flank of one of these landforms (Fig. 1c).
142 The location of site C on the crest of the MSGL means that the thin sections represent a vertical
143 section through the landform and therefore provide a valuable insight into the processes which may
144 have occurred during the formation of this landform. The terminology used to describe the various
145 microtextures developed within these sediments follows that proposed by van der Meer (1987,
146 1993) and Menzies (2000) with modifications. Microstructural maps and quantitative data for the
147 clast microfabrics (Figs. 2 to 7) developed within the till were obtained using the methodology of
148 Phillips *et al*. (2011) (also see Vaughan-Hirsh *et al*., 2013; Neudorf *et al*., 2013; Gehrmann *et al*.,
149 2017; Phillips *et al*., 2013, 2018; Brumme, 2015). During this process the relationships between
150 successive generations of clast microfabrics (S1 oldest to Sn youngest) and other microstructures
151 (e.g. plasmic fabrics, turbate structures, folds, faults, shears…etc) present within the diamicton are
152 determined, allowing a detailed relative chronology of fabric development to be established,
153 enabling the investigation of the complex polyphase deformation histories recorded in these
154 deposits (see Phillips *et al*., 2011 for details of this process). Each thin section was divided into 16
155 rectangular areas (A to P on Figs. 2 to 7) and the orientation of the long axes of the clasts (skeleton
156 grains) plotted on a series of rose diagrams and the eigenvalues (E1, E2) calculated for each area
157 using the commercial software package StereoStat by RockWare ™ (see Fig. 2 to 7). In order to
158 assess the effects of grain size on clast microfabric development within tills, the long axis data were
159 divided into three sets: *(i)* grains < 0.25 mm in length (fine-sand and below); *(ii)* grains between 0.25
160 to 0.5 mm in size (medium-sand); and *(iii)* grains over > 0.5 mm in length (coarse-sand and above).
161 The resultant data sets were plotted on a series of histograms and rose diagrams to highlight any
162 variation in clast size versus long axis orientation.

163   In conjunction with the manual microstructural mapping methodology (Phillips *et al.*, 2011)

164   an automated approach using ArcGIS line density tools was conducted on selected thin sections

165   (X1M, Y1M, Z1M) to provide a robust, objective interpretation of the clast microfabrics. These

166   automated tools allow the calculation of the magnitude of long axes per unit area within a thin

167   section and was applied to each of the clast microfabrics. The variation in density (mm^2) of the clasts

168   defining each microfabric was calculated with the resulting output raster files providing a map of

169   relative intensity of clast microfabric for each thin-section (Fig. 8).

4. Results of the micromorphological and microstructural analysis

4.1. Composition and provenance of the till

172   In thin section (C1M, C2M, C3M, C4M, C5M, C6M) the till is massive, lacking any obvious

173   stratification (e.g. bedding) or other primary structure. It is composed of fine- to medium-grained,

174   open-packed, matrix-supported, silty sand (Figs. 2-7) containing scattered, angular to well-rounded

175   granule, to small pebble-sized rock fragments composed of sedimentary rocks (siltstone, sandstone,

176   mudstone, indurated quartz-arenite, bioclastic limestone, micritic limestone), igneous (biotite-

177   granite, muscovite-granite, alkali granite, micrographic intergrowth, altered volcanic rocks) and

178   metamorphic rocks (amphibolite, biotite-schist) (Table 1). Angular to subangular, coarse-silt to sand-

179   sized grains within the till matrix are composed of monocrystalline quartz and feldspar (plagioclase,

180   K-feldspar). The compositional data support the conclusion of Spagnolo *et al.* (2016) that the till was

181   laid down by ice advancing from the NW and contains far-travelled material derived from Palaeozoic

182   sedimentary sequences within the Baltic Basin and crystalline basement rocks from Scandinavia;

183   similar till compositions have also been reported from Germany and Denmark (Piotrowski, 1994a, b;

184   Kjær *et al.*, 2003).

185   The thin sections reveal that the till is compositionally, essentially homogenous with only a

186   slight increase in the proportion of limestone and fine carbonate grains downwards through the

187   sequence (Table 1). This increase in detrital carbonate is accompanied by the appearance of small,

188   irregular patches of a micritic carbonate cement which appears to replace the clay within the matrix

189   (Figs. 9a, b, c; red areas on Figs. 4 to 7). Small, rounded to irregular voids and fractures within the till

190   are lined or filled by massive to very finely laminated, highly birefringent clay (Figs. 9d, e, f). These

191   clay-filled features form between 5 and 15% (visual estimate) of the matrix, and locally (e.g. C1M)

192   define a weakly developed subhorizontal "foliation". The dark orange-brown clay is petrographically

193   similar to clay cutan within soils, suggesting that it was deposited by water flowing through the till

194   matrix, with the laminated nature of these fines recording several phases of fluid flow.

4.2. Microstructures developed in response to subglacial deformation

Microstructural analysis of the thin sections (C1M to C6M; Figs. 2 to 7, respectively) has revealed that the tills possess five successive generations of clast microfabric (S1 to S5) defined by the preferred shape alignment of elongate coarse silt to sand-grade clasts. The relative intensity of these microfabrics varies across the thin section, reflecting the heterogeneous nature of shearing within the glacier bed. The spacing of the microfabric domains is controlled by the overall grain size of the diamicton and occurrence of coarse-sand to small pebble-sized clasts which acted as rigid bodies during deformation. Although the results of detailed microfabric analysis described below focus upon site C, comparable fabric geometries have been observed in the thin sections from sites X, Y and Z (Fig. 8).

The earliest microfabric is a very poorly developed/preserved, typically down-ice dipping S1 fabric (purple on Figs. 2 to 7). This fabric, where present, is cross-cut by a highly heterogeneous, subhorizontal to very gently inclined S2 fabric (pale green on Figs. 2 to 7). In the upper part of the till (C1M to C3M) S2 occurs within weakly to moderately well-defined, lenticular bands (Figs. 2 and 3) and is interpreted as having formed coplanar to the bed of the overriding ice. A weakly developed asymmetrical to S-shaped fabric geometry (S-C-type fabric) within the bands of S2 records a sinistral (in this plane of section) SE-directed (down-ice) sense of shear (Figs. 3, 4, 5 and 7). Lower within the till sequence (C4M to C6M), however, the banded appearance of S2 is less apparent as this fabric has been variably overprinted by a later foliation (see below).

Poorly to rarely developed, arcuate grain alignments and turbate structures (van der Meer, 1983; Menzies, 2000) occur within the microlithons between S1 and S2, and are locally truncated against these foliations. Turbate structures are interpreted to have formed where larger clasts rotate through angles up to, and greater than 360° entraining the adjacent finer grained matrix (van der Meer, 1993, 1997; Menzies, 2000; Hiemstra and Rijsdijk, 2003; Lea and Palmer, 2014). Their variable preservation within the S1 and S2 microlithons suggests that this rotational deformation occurred prior to the imposition of the clast microfabrics.

The dominant fabric is an up-ice dipping S3 microfabric (dark green on Figs. 2 to 7). This fabric cross-cuts S2, with the earlier S1 being preserved within the microlithons separating the S3 domains. In detail S3 is composed of two components: *(i)* a moderately to steeply (40° to 50°) up-ice dipping foliation; and *(ii)* a more gently inclined (20° to 40°) foliation (Figs. 2, 3 and 4). The later, down-ice dipping (20° to 40°) S4, microfabric is heterogeneous, potentially reflecting the partitioning of deformation into increasingly narrower zones of shear during the later stages of bed deformation. S2 and S3 are deformed by S4 resulting in a distinctive S-shape to sigmoidal fabric geometry

comparable to an extensional crenulation cleavage (ECC fabric) associated with extensional shears formed in brittle-ductile shear zones (Passchier and Trouw, 1996). This fabric geometry once again records a sinistral, SE-directed sense of shear (Figs. 2, 3, 5 and 6) consistent with the ice movement direction in the study area (see Fig. 1c).

The same microfabric relationships (S2 to S4) were recorded in all thin sections (see Figs. 2 to 7) indicating that not only were these fabrics developed in response to the same overall stress regime, but that this regime (dominated by SE-directed shear) was maintained throughout the deposition of the entire till sequence. This conclusion is supported by the rose diagrams shown on Figs. 2 to 7 which indicate that the orientation of S2, S3 and S4 remains essentially constant throughout the till with very little modification due to compaction. The geometry of these fabrics is consistent with their development in response to the formation of Y (S2), R (S3) and P-type (S4) Reidel shears (c.f. Spagnolo *et al.*, 2016) within a subhorizontal subglacial shear zone formed beneath the overriding OPIS (Fig. 10).

S1 to S4 shear related fabrics are cross-cut by a subvertical, anastomosing S5 fabric which locally wraps around the larger granule to pebble sized clasts (Figs. 3 to 7). The overall intensity of this fabric increases down-wards through the till (C2M to C6M) where it locally overprints the earlier developed foliations. The patches of micritic carbonate within the matrix of the till occur within, or close to the areas possessing a well-developed S5 fabric (Figs. 4 to 7), indicating that development of this fabric may have accompanied the passage of $CaCO_3$-bearing fluids through the sediment (see section 5).

4.3. Effect of grain size on microfabric development

To assess the effects of grain size on clast microfabric development the long axis data were divided into three sets: *(i)* < 0.25mm (fine-sand and below); *(ii)* 0.25 to 0.5 mm (medium-sand); and *(iii)* > 0.5 mm in size (coarse-sand and above). The orientation data derived for these sets are shown on Figs. 11 and 12. Although the same clast microfabrics are present within all three clast sizes (Fig. 12), they are most pronounced within the finer grained components with the data highlighting a change in the orientation of the dominant fabric downwards through the till (Fig. 11). In the "upper" part of the till (C1M, C2M, C3M), the up-ice dipping S3 is dominant and its relative intensity appears to increase downwards (Figs. 11 and 12). This variation in the intensity of fabric development may record a progressive change in the relative intensity of deformation/magnitude cumulative strain imposed at the ice/bed interface during till accretion (Boulton, 1996; Boulton and Hindmarsh, 1987; Evans *et al.*, 2006 and references therein). In the "lower" part of the till (C4M, C5M, C6M) the relative intensity of the shear fabrics decreases with S3 being replaced by the down-ice dipping S4 as the dominant

261 foliation (Figs. 11 and 12). However, the fabrics (S2, S3, S4) in the "lower" part of the till have been

262 strongly modified by the imposition of S5 (see Figs. 5 to 7). The boundary between these "upper"

263 and "lower" till units appears to be relatively sharp and located between samples C3M and C4M.

264 However, no obvious boundary was observed at this level within the trench (see Fig. 1c).

265 5. Variation in microfabric intensity within the OPIS till

266 The results of the micromorphological study indicate that there is a significant variation in the

267 relative intensity of microfabric development within the till.

268 *5.1. Automated clast microfabric analysis*

269 The results of the automated approach to quantify the variation in clast microfabric strength are

270 shown in Fig. 8. The thin sections used (X1M, Y1M, Z1M) represent a traverse down the flank of an

271 MSGL (Fig. 1c) designed to investigate any potential lateral changes in the style and relative intensity

272 of fabric development across this subglacial landform. Importantly this method has revealed a

273 similar pattern of microfabric development within each of the thin sections as those analysed using

274 manual methodology of Phillips *et al*. (2011) (compare Figs. 2, 3 and 8). It is clear from Fig. 8 that all

275 of the microfabrics (S2, S3, S4, S5) are heterogeneously developed, even within a single thin section,

276 reflecting the partitioning of deformation on a microscale within the bed of the OPIS. S3 is the

277 dominant fabric and is most intensely developed within the samples located close to the crest of the

278 MSGL (X1M) and within the adjacent trough (Z1M) (Fig. 8). In contrast, both S2 and S4 are more

279 weakly developed on top of the landform (X1M) in comparison to its flanks (Y1M, Z1M) the strength

280 of S5 increases down the flank of the MSGL towards the adjacent trough.

281 *5.2. Statistical clast microfabric analysis*

282 The variation in E1 eigenvalues calculated for the samples from site C (C1M to C6M) are illustrated

283 on Fig. 13. The red colours represent areas of the thin sections with higher E1 values (0.65-0.68),

284 corresponding to relatively stronger fabric development, and purple lower values (0.53-0.51),

285 highlighting areas where the clast microfabrics are less well-developed. This approach reveals that

286 fabric strength not only varies within an individual thin section, but also vertically through the till

287 (Figs. 13 and 14a), supporting the results of the grain size fabric analysis (Figs. 11 and 12). The

288 eigenvalues are typically higher within the upper part of the till (C1M, C2M, C3M; Table 2), recording

289 an overall relative increase in fabric strength upwards through the till (Fig. 13); although sample C3M

290 has the highest E1 values compared to the other two samples. In contrast, the lower three samples

291 all possess low eigenvalues (Figs. 13 and 14a; Table 2) corresponding to much weaker fabric

292 strengths. Although it is tempting to suggest that the lower part of the till is more weakly deformed,

293 this may simply reflect the overprinting of the earlier shear related fabrics (S2 to S4) by the later S5

294 microfabric (see Figs. 5 to 7).

295   The eigenvalues (< 0.6; Fig. 13 and Table 2) can be used to suggest that the amount of shear

296 being transmitted into the bed of the OPIS was relatively low. In the absence of any obvious strain

297 markers (e.g. deformed clasts known to have been originally circular in shape) estimating the

298 magnitude of the shear strains imparted by the overriding ice remains problematic. Several workers

299 have used the relative abundance of selected microstructures (e.g. microshears, grain stacks) as a

300 proxy for estimating strain in subglacial traction tills (Larsen *et al.*, 2006, 2007; Narloch *et al.*, 2012).

301 However, the development of such features can be strongly lithologically controlled; e.g.

302 microshears defined by a unistrial plasmic fabrics will only form in clay-rich sediments. Furthermore,

303 their identification is qualitative and potentially subjective (Leighton *et al.*, 2012; Neudorf *et al.*,

304 2013). Phillips *et al.* (2013) suggested that shear strain curves established from experimental

305 deformation studies (e.g. Thomason and Iverson, 2006) can be used to provide a minimum estimate

306 of the shear strains experienced by subglacial traction tills. In the absence of strain curves for a

307 range of naturally occurring tills, the potential closest "match" to the sand-rich OPIS till is the

308 Douglas till strain curve of Thomason and Iverson (2006) (Fig. 14b). When projected onto this curve

309 the range of average E1 values for the OPIS till suggests that microfabric development occurred in

310 response to shear strains of < 15 (Fig. 14b). If this approach is valid then it supports the suggestion

311 that the amount of shear being transmitted into the bed of the OPIS by the overriding ice was

312 relatively low (cf. Larsen *et al.*, 2007; Narloch *et al.*, 2012; Phillips *et al.*, 2013).

313 6. Implications for bed deformation beneath the OPIS

314 *6.1. Foliation development in response to progressive simple shear*

315 Results of this detailed microscale study reveal that deformation within the bed of the OPIS was

316 dominated by foliation development which lacked any concomitant folding and/or faulting (c.f.

317 Spagnolo *et al.*, 2016). The microfabrics define a set of up-ice and down-ice dipping Riedel shears (S3

318 – P-type and S4 – R-type shears; Fig. 10), as well as a subhorizontal shear foliation (S2 – Y-type

319 shears; Fig. 10) with S2 having formed parallel to the ice-bed interface (Figs. 10 and 15). The

320 consistency of the geometry and orientation (Figs. 2 to 7, and 15) of these microfabrics indicate that

321 not only did subglacial deformation occur in response to the same overall stress regime, but also

322 that they have undergone very little modification due to compaction/loading subsequent to

323 formation which would have led to the "flattening" (decrease in dip) of the fabrics at depth within

324 the till (see rose diagrams on Fig. 15). The consistency of the data also indicates that ductile shearing

beneath the OPIS was spatially uniform and occurred within an essentially subhorizontal subglacial shear zone (see Fig. 10). Furthermore kinematic indicators (S-C and ECC-type microfabrics) record a consistent SE-directed (sinistral) sense of shear, coincident with the long axes of the MSGL and regional pattern of ice flow across the Wielkopolska Lowland (Przybylski, 2008; Spagnolo *et al.*, 2016).

The cross-cutting relationships displayed by S2, S3 and S4 can be interpreted as reflecting temporal changes in the style of deformation being accommodated within the till. However, the consistent SE-directed sense of shear recorded by these fabrics clearly indicates that they formed in response to the same overall stress regime imposed during a single progressive shear event rather than completely separate phases of deformation. S2 defines a series of subhorizontal Y-type shear planes indicating that the earlier stages of ductile deformation were dominated by shear occurring coplanar to the base of the overriding ice. S2 is cross-cut by the up-ice dipping S3 foliation which defines a number of P-type shears indicating that initial layer-parallel shear was superseded by compressional deformation. S3 is then cross-cut by the later down-ice dipping S4 which records the nucleation and growth of apparently late-stage extensional R-type shears within the bed of the OPIS. The same relationships were observed in all the thin sections and are interpreted as recording temporal changes in the style of deformation imposed on the till during its evolution.

6.2. Clast microfabric development in tills

The individual clast microfabrics within the OPIS till formed as a result of the passive rotation of coarse-silt to sand-grade particles into the plane of the developing foliation(s) (Fig. 16) reflecting the stress field imposed by the overriding ice (c.f. Hiemstra and Rijsdijk, 2003; Phillips *et al.*, 2011). Once aligned, further rotation will cease and the clasts will maintain their preferred alignment unless there is a change in the orientation of this stress field within the evolving Reidel shears. As deformation continues, the microfabric domains defining the shear fabrics will propagate laterally as more grains become aligned. Further deformation within the microshears will be accommodated by either sliding of the grains past one another (Fig. 16a) and/or the partitioning of shear into the intervening finer grained matrix. If the matrix contains a significant modal proportion of clay minerals then this may lead to the formation of a unistrial plasmic fabric (van der Meer, 1993; Menzies, 2000; 2012; Hiemstra and Rijsdijk, 2003) coplanar to the evolving clast microfabric.

The grain size of the sediment also influenced microfabric development with preferred clast alignments being most apparent within the finer grained (< 0.25 µm; 0.25 to 0.5 µm) components (matrix) of the till (Figs. 11 and 12). During deformation, it is suggested that the larger grains (cobbles, pebbles) were the first to stop rotating, becoming "locked" into position with subsequent

358   increments of deformation being partitioned into the still "active" matrix (c.f. Evans *et al*., 2016;

359   Evans, 2018). Consequently the matrix of the till continued to respond to shear long after the larger

360   clasts have become immobile and therefore provide the most complete record of subglacial

361   deformation. Results from several micromorphological studies (Phillips *et al*., 2011, 2013, 2018)

362   suggest that larger sand, granule to pebble sized clasts (where present) control the spacing of the

363   developing microfabric domains, influencing the pattern of deformation partitioning within the till

364   (Fig. 16). By the way of analogy, in metamorphic rocks the mica domains, defining the schistosity in

365   amphibolite facies pelitic rocks (metamorphosed mudstones), are thought to nucleate upon the

366   margins of ridged porphyroblasts (e.g. garnet), propagating laterally away from these relatively

367   higher strain areas as deformation/fabric development continues (Bell, 1985; Bell and Rubenach,

368   1983; Bell *et al*., 1986; Vernon, 1989; Johnson, 1990). It is possible that a similar process also occurs

369   in tills with the microfabrics nucleating upon the larger clasts due to the concentration of strain

370   along the margins of these rigid grains. The evolving foliation then propagates away from this

371   nucleation point into the adjacent matrix. The presence of larger rigid clasts will affect/distort (on a

372   microscale) the stress and strain field imposed upon the till matrix (Fig. 16b) leading to the

373   development of anastomosing microfabric, wrapping around these coarse sand to pebble-sized

374   grains (Fig. 16c).

375   Evans *et al*. (2006) suggested that deformation (fabric development, folding, faulting) within

376   the bed will only occur when the intergranular pore water pressure falls and a coherent "till-matrix

377   framework" develops (also see Evans, 2018). Consequently, the nucleation and subsequent

378   evolution of the clast microfabrics is likely to be controlled by the water content and packing of the

379   till. However, increasing the packing of the constituent grains within the sediment will lead directly

380   to an increase in its peak frictional strength and its resistance to deformation, which may be

381   overcome by an increase in the magnitude of the imposed shear stress. Consequently, there is likely

382   to be a critical range in intergranular porewater content/pressure and sediment packing for foliation

383   development to occur within tills. For example, foliation development within a "dry" till comprising

384   dense, closely packed grains will be limited due to the high percentage of inter granular contacts

385   restricting grain rotation. In contrast, a shear stress applied to a water-saturated till is likely to

386   induce dilation or even localised liquefaction which will not only inhibit fabric development, but also

387   lead to the overprinting of earlier developed microstructures (Evans *et al*., 2006; Phillips *et al*., 2011;

388   2013; 2018). The inherent spatial variation in the water content and packing of the till will lead to

389   the small-scale partitioning of deformation and heterogeneous fabric development within the bed of

390   the OPIS (Figs. 2 to 8).

6.3. Evidence of intergranular fluid flow and dewatering of the bed

The matrix of the till forming the bed of the OPIS contains clay-lined or filled voids, intergranular pore spaces and fractures (Fig. 9). The clay is petrographically similar to clay cutan within soils, suggesting that it was deposited by water flowing through the till so that the laminated nature of these fines records several phases of fluid flow. Although clay infiltration can occur during pedogenic processes, these features occur well below the base of the modern soil (see Fig. 1d) indicating that it was unrelated to recent pedogenic processes. Observations from contemporary (Alley *et al.*, 1986; Tulaczyk *et al.*, 1998) and palaeo (Ó Cofaigh *et al.*, 2007) ice stream beds indicate that the tills are typically highly porous and weak, with a water content close to the liquid limit. The clay within the OPIS till forms between 5 and 15 % of the matrix and is observed variably infilling intergranular pore spaces, consistent with the nature of tills described from modern ice stream beds (Alley *et al.*, 1986; Tulaczyk *et al.*, 1998; Ó Cofaigh *et al.*, 2007). Significant compaction of the OPIS till would have led to an increase in its packing, reducing in its porosity and permeability. Consequently the preferred interpretation is that fluid flow and clay infiltration probably occurred shortly after till deposition; a conclusion supported by the dark coloration of the clay resulting from its replacement by Fe/Mn during 'maturation' (van der Meer, 2007 pers. comm.; Phillips and Auton, 2008).

In the lower part of the OPIS till the earlier shear fabrics (S2 to S4) are variably overprinted by S5 (Fig. 15). The intergranular clays show very little, if any, evidence of disruption/fragmentation suggesting that they post-date any significant deformation and/or reorganisation of the structure and packing of the till during the imposition of S5. Consequently, it is suggested that S5 pre-dated the intergranular fluid flow and clay infiltration, with the imposition of this late stage foliation probably accompanying the dewatering of the till driven by the ice overburden pressure; a conclusion supported by the relative increase in the intensity of this fabric downward through the till (Fig. 15). The micritic carbonate within the matrix of the till (red areas on Fig. 15) exhibits a close spatial relationship to S5, indicating that diagenesis may have accompanied the imposition of this fabric and recording the passage of a $CaCO_3$-bearing fluid phase through the sediment. If the carbonate was pedogenic then it should increase upwards towards the base of the modern soil, possibly forming a calcified crust at the base of the soil profile. Several studies have examined the dissolution of carbonate in glacial environments (e.g. Fairchild *et al.*, 1993; 1994; Menzies and Brand, 2007) with McGillen and Fairchild (2005) suggesting that this process may be facilitated by the crushing and comminution of carbonate grains within subglacial traction tills. Menzies and Brand (2007) argued that carbonate cementation of ice-contact sands and gravels exposed within core of a large drumlin in New York State occurred in response to a reduction in hydrostatic pressure and release of CO_2 from the meltwater escaping from beneath the Laurentide Ice Sheet. Consequently, it

13

425 is possible that carbonate diagenesis within the OPIS till may have occurred penecontemporaneous
426 with subglacial deformation. As noted above, S5 clearly overprints the shear related fabrics within
427 the till and therefore post-dated subglacial shearing. However, due to the potentially diachronous
428 nature of deformation within the OPIS till, dewatering and imposition of S5 within the structural
429 lower parts of the sequence is thought to have been initiated whilst subglacial shearing was
430 continuing at a higher level within the bed (Fig. 15) (see below).

431 *6.4. The nature of bed deformation beneath the OPIS: deformation*
432 *partitioning or incremental progressive simple shear during till accretion*
433 Spagnolo *et al.* (2016) argued that the till beneath the OPIS was being continuously accreted at the
434 top of a shallow-deforming bed (cf. Tulaczyk, 1999; Iverson *et al.*, 1998; Fuller and Murray, 2000;
435 Piotrowski *et al.*, 2001, 2004; Evans *et al.*, 2006; Cuffey and Paterson, 2010; Iverson, 2011; Evans,
436 2018). However, the possibility that pervasive bed deformation may have occurred to greater depths
437 beneath this ice stream needs to be considered. Quantitative data presented here provides evidence
438 that fabric (S2, S3, S4, S5) strength varies (on a microscale) both laterally and vertically within the
439 bed of the OPIS (Figs. 13 and 15). If this variation in fabric strength can be used as a proxy for the
440 relative intensity of shear imposed on the till it may reflect either: *(i)* the partitioning of deformation
441 within the subglacial shear zone formed beneath this ice stream, within the deforming bed and
442 potentially encompassing the entire thickness of the till; or *(ii)* the variation in the magnitude of the
443 shear being transmitted into the deforming bed during the progressive accretion of the OPIS till.

444 A number of studies have suggested that subglacial shear zones migrate through the bed
445 due to spatial and temporal fluctuations in water content/pressure (Tulaczyk, 1999; Truffer *et al.*,
446 2000; Evans *et al.*, 2006; Kjær *et al.*, 2006; Lee and Phillips, 2008) and/or the ability of these
447 sediments to drain intergranular porewater (Piotrowski *et al.*, 2004). Deformation within the shear
448 zone can either be 'pervasive' (homogeneous) and transmitted throughout the entire bed (van der
449 Meer *et al.*, 2003; Menzies *et al.*, 2006), or heterogeneous where the bed comprises a 'mosaic' of
450 actively deforming and stable (non-deforming) zones (Piotrowski and Kraus, 1997; Piotrowski *et al.*,
451 2004; Lee and Phillips, 2008). Tills within the beds of ice streams are thought to be water-saturated
452 and weak (Alley *et al.*, 1986; Tulaczyk *et al.*, 1998; Ó Cofaigh *et al.*, 2007), and therefore able to
453 accommodate a significant proportion of the forward motion of the overriding ice. The consistency
454 of the orientation and geometry of the shear fabrics (S2 to S4; Fig. 15) throughout the OPIS till,
455 coupled with the very low preliminary estimates of shear strain (Fig. 14) may be used to support the
456 presence of weak, water-saturated sediments beneath this palaeo-ice stream, facilitating the
457 transmission of shear throughout its entire bed (Hart and Boulton, 1991; van der Wateren *et al.*,
458 2000; van der Meer *et al.*, 2003; Menzies *et al.*, 2006). In detail, the relative intensity of the shear

14

fabrics vary both laterally and vertically (Figs. 8 and 13). However, there is no obvious macroscale evidence for the presence of a significant décollement surface (thrust) within the bed of the OPIS till (see Fig. 1d). So as a result, it cannot be argued that forward motion of the OPIS was accommodated by deformation at a deeper level within the sediment pile (Fig. 17a). Consequently, variations in the relative intensity of foliation development within the OPIS till is more likely to record the small-scale partitioning of deformation during subglacial shear.

The deforming bed model for glacier motion predicts an increase in cumulative strain upwards toward the ice-bed interface (Boulton, 1986; Boulton and Hindmarsh, 1987; Evans et al., 2006) with deformation being accommodated by a weak, water-saturated layer located immediately adjacent to, or at the ice-bed interface (Fig. 17b). The continuous deposition of a soft (weak), compositionally homogenous (well-mixed; see section 4.1) till layer at the top of the bed of the OPIS (Spagnolo et al., 2016) means that over time deformation will have progressively shifted upwards as till accreted (Fig. 17b). The trenches in the study area reveal that the till sequence beneath the OPIS is at least 1.2 to 1.4 m thick, with Ground Penetrating Radar data indicating that the diamicton may be in the order of 2 to 3 m thick (Spagnolo et al., 2016). The soft deforming layer responsible for till accretion at the top of this sequence is likely to have only been a few tens of centimetres thick (Menzies 1982; Alley et al., 1986, 1987; Boulton, 1996; Hindmarsh, 1998; Larsen et al., 2004, 2007; Evans et al., 2006; Stokes et al., 2013a) and localised in nature reflecting the spatial and temporal changes in bed conditions. Phillips et al. (2018) suggested that the term 'transient mobile zone' for this actively deforming layer in order to emphasize the spatial and temporal variations in subglacial deforming bed processes proposed by a number of researchers (e.g. Piotrowski and Kraus, 1997; Boyce and Eyles, 2000; van der Meer et al., 2003; Larsen et al., 2004, 2007; Piotrowski et al., 2004, 2006; Evans et al., 2006; Meriano and Eyles, 2009; Evans, 2018). The focusing of deformation into this water-saturated mobile layer would have effectively switched off deformation at a deeper level within the bed. As a consequence of this progressive till accretion-deformation, the relative age of subglacial shearing beneath the OPIS would be diachronous, becoming progressively younger toward the top of the bed. The observed vertical variation in the relative intensity of the shear fabrics (S2 to S4; Figs. 13 and 15) may therefore be interpreted as recording changes in the magnitude of the cumulative strain being recorded by the till during this accretion-deformation process (Fig. 17c) (cf. Larsen et al., 2004). The variation in fabric strength may reflect the degree of coupling between the ice and the underlying bed; the greater the fabric intensity the higher the degree of ice-bed coupling and transmission of shear into the bed.

491   Preliminary estimates of the shear strains involved are low (< 15; Fig. 14b) indicating that the

492   amount of shear being transmitted into the bed of the OPIS was relatively small (cf. Larsen *et al.*,

493   2006; Narloch *et al.*, 2012; Phillips *et al.*, 2013). Consequently, fast flow of this ice stream would

494   have been largely accommodated by either basal sliding and/or flow deformation within a weak,

495   water-saturated layer located at the top of the accreting till sequence (Evans *et al.*, 2006; Phillips *et*

496   *al.*, 2013; Spagnolo *et al.*, 2016). Evidence of the latter is potentially provided by the rotational

497   turbate structures (van der Meer, 1993, 1997; Menzies, 2000; Hiemstra and Rijsdijk, 2003). These

498   structures are truncated by the shear fabrics, indicating that rotational deformation occurred prior

499   to foliation development within the OPIS till. Turbate structures form where larger clasts are able to

500   rotate through angles of up to, or > 360°, entraining the adjacent finer grained matrix (van der Meer,

501   1993; Menzies, 2000; Lachniet *et al.*, 2001; Hiemstra and Rijsdijk, 2003; Phillips, 2006; Lea and

502   Palmer, 2014). This requires either very high shear strains or the lowering of the strength of the

503   sediment enabling clast rotation at the much lower strains (Evans *et al.*, 2006), the latter being more

504   likely due to the very low shear strain estimates obtained for the OPIS till. The presence of an active

505   layer at the top of the bed would have markedly reduced or even prevented transmission of the

506   shear into the underlying till. Furthermore, this layer is likely to have been highly mobile, facilitating

507   the advection of well-mixed, far-travelled sediment down-ice and the continuous accretion of till at

508   the top of a shallow deforming bed (Spagnolo *et al.*, 2016). Spatial and temporal fluctuations in the

509   water content within this active layer will have affected the degree of ice-bed coupling, leading to

510   the observed complex pattern of cumulative strain (Figs. 13, 14 and 15).

511   Microtextural evidence (sections 5 and 6) indicates dewatering, consolidation and

512   cementation of the OPIS till. These processes could have led to an increase in the shear strength of

513   the till potentially resulting in the increased "stabilisation" of the sediment within the cores of the

514   MSGL as they grew beneath the OPIS. Till consolidation or the presence of a relatively hard/stiff core

515   has been invoked in the initiation of some subglacial landforms (e.g. Menzies and Brand 2007;

516   Menzies *et al.*, 2016), although this concept is challenged by the regular spatial distribution of these

517   landforms (e.g. Spagnolo *et al.*, 2016). In specific case presented here, the results suggest that till

518   consolidation may have been initiated at a lower level within the MSGL whilst till deformation and

519   accretion continued above (see sections 6.3. and 6.4), thus providing no support for the idea that a

520   stiffened core is required for MSGL initiation.

521   Although it is acknowledged that the detailed micromorphological/microstructural study

522   presented here has largely focused upon a single site (site C), the results are applicable to the wider

523   footprint of the OPIS as well as other contemporary and palaeo-ice streams. Deformation beneath

glaciers and ice sheets is widely viewed as being dominated by simple shear within a subglacial shear zone (e.g. van der Wateren *et al.*, 2000; Hart, 2007; Lee and Phillips, 2008; Benn and Evans 2010). The style of deformation identified within the bed of the OPIS is consistent with this assumption, with comparable microscale shear fabrics being recognised in subglacial traction tills (sensu Evans *et al.*, 2006) from other glaciated terrains (e.g. Germany - van der Wateren *et al.*, 2000; England (Norfolk) - Vaughan-Hirsh *et al.*, 2013; British Columbia, Canada - Neudorf *et al.*, 2013; Central Poland - Narloch *et al.*, 2012, 2013; Baltic Coast, northern Germany - Brumme, 2015; Gehrmann *et al.*, 2017; Scotland - Phillips *et al.*, 2011, 2018; Switzerland - Phillips *et al.*, 2013). In structural geology, Pumpelly's rule states that small deformation structures are a key to understanding the structural evolution of an area as they mimic the styles and orientations of a larger-scale structures of the same generation. Consequently, the geometry and the relationships displayed between the range of microscale (and macro-) structures found within subglacially deformed sediments can not only be used to establish the overall stress regime responsible for deformation (e.g. van der Wateren *et al.*, 2000; Vaughan-Hirsh *et al.*, 2013; Gehrmann *et al.*, 2017), but also aid in the reconstruction of the regional pattern of ice movement (e.g. Brumme, 2015). The bed of the OPIS across the Wielkopolska Lowland region is very gently undulating (Fig. 1c) (Przybylski, 2008; Spagnolo *et al.*, 2016) and can, in general, be considered to be represented by an essentially subhorizontal ductile-brittle shear zone. The thick (c. 30 m) sequence of Quaternary sediments which blanket the area result in an absence of any major bedrock highs which would have imposed significant changes on the stress regime active within the bed of this palaeo-ice stream. Furthermore, gravel to cobble-sized clasts, which would have locally influenced (modified) microscale fabric development, are rare with the OPIS till. Consequently, the proposed model of progressive ductile shearing during till accretion is considered to be applicable across the bed of the Odra palaeo-ice stream with changes in microfabric geometry reflecting local changes in the physical properties of the sediment (e.g. grain size, porewater content) during fast ice flow.

7. Conclusions

The detailed microstructural study of the thick subglacial traction till formed within the bed of the Weichselian Odra palaeo-ice stream contributes to our understanding of the deformation processes occurring within its bed and it how it evolved over time.

- The massive, compositionally homogenous nature of the till indicates that the sediment being accreted to the bed was well-mixed and included far travelled material derived from Palaeozoic rocks of the Baltic Basin and crystalline basement of Scandinavian, consistent with the till being laid down by ice advancing from the NE.

- Deformation within the bed of the ice stream was dominated by foliation development (S1 to S5) recording progressive ductile shearing within a subhorizontal subglacial shear zone. Cross-cutting relationships displayed by these shear fabrics (S2, S3 and S4) reflect temporal changes in the style of deformation being accommodated within the till during a single progressive shear event as the till accreted vertically. Kinematic indicators (S-C and ECC-type microfabrics) within the till record a consistent SE-directed (sinistral) sense of shear coincident with the regional pattern of ice flow across the Wielkopolska Lowland.

- The clast microfabrics reflect the stress field imposed by the overriding ice and form as a result of the passive rotation of detrital grains into the plane of the developing foliation(s). Larger clasts (pebbles, cobbles) become "locked" into position at an earlier stage within the deformation history and with subsequent shear being partitioned into the matrix of the till. These larger clasts then control the partitioning of deformation within the till and the spacing of the evolving microfabric domains.

- Evidence of intergranular pore water flowing through the bed of the OPIS is provided by the presence of clay-filled pore spaces within the till matrix having potentially occurred during or shortly after deposition. Further evidence of fluid flow through the bed is provided by the anastomosing, subvertical S5 fabric which formed in response to the dewatering and consolidation of the till in response to deposition from the deforming layer and final shutdown of the ice stream. Dewatering of the bed was accompanied by the growth of diagenetic micritic carbonate indicating that the escaping fluid contained dissolved $CaCO_3$ derived from the dissolution of detrital limestone.

- Bed deformation beneath the OPIS occurred in response to incremental progressive simple shear during till accretion. The relative age of deformation was diachronous (younger towards the top of the bed) as a thin deforming layer migrated progressively upwards in response to till accretion at the top of the ice stream bed. Focusing of deformation into this "active" layer or "transient mobile zone" effectively switched off deformation deeper within the bed. Variations in the relatively intensity of the microfabrics may record changes in the magnitude of the cumulative strain being imposed on the till during this accretion-deformation process and the degree of coupling between the ice and the underlying bed. Preliminary estimates of the shear strains involved are low, indicating that the amount of shear being transmitted into the bed of the OPIS was relatively small. This has implications for the mechanism responsible for the forward motion of this palaeo-ice stream.

8. Acknowledgements

9. References

Alley, R.B., 1989. Water pressure coupling of sliding and bed deformation: 1. Water system. Journal of Glaciology 35, 108-118.

Alley, R.B., Blankenship, D.D., Bentley, C.R., Rooney, S.T., 1986. Deformation of till beneath ice stream B, West Antarctica. Nature 322, 57-59.

Alley, R.B., Blankenship, D.D., Bentley, C.R., Rooney, S.T., 1987a. Till beneath ice stream B: 3. Till deformation: evidence and implications. Journal of Geophysical Research 92, 8921-8929.

Alley, R.B., Blankenship, D.D., Rooney, S.T., Bentley, C.R., 1987b. Till beneath ice stream B: 4. A coupled ice-till flow model. Journal of Geophysical Research 92, 8931-8940.

Bamber, J.L., Vaughan, D.G., Joughin, I., 2000. Widespread complex flow in the interior of the Antarctic Ice Sheet. Science 287, 1248–1250.

Baroni, C., Fasano, F., 2006. Micromorphological evidence of warm-based glacier deposition from the Ricker Hills Tillite (Victoria Land, Antarctica). Quaternary Science Reviews. 25, 976-992.

Bell, T.H., 1985. Deformation partitioning and porphyroblast rotation in metamorphic rocks: a radical reinterpretation. Journal of Metamorphic Geology 3, 109-118.

Bell, T.H., Rubenach, M.J., 1983. Sequential porphyroblast growth and crenulation cleavage development during progressive deformation. Tectonophysics 92, 171-194.

Bell, T.H., Rubenach, M.J., Fleming, P.D., 1986. Porphyroblast nucleation, growth and dissolution in regional metamorphic rocks as a function of deformation partitioning during foliation development. Journal of Metamorphic Geology 4, 37-67.

617 Bennett, M.R., 2003. Ice streams as the arteries of an ice sheet: their mechanics, stability and
618 significance. Earth Science Reviews 61, 309–339.

619 Bingham, R.G., Vaughan, D.G., King, E.C., Davies, D., Cornford, S.L., Smith, A.M., Arthern, R.J.,
620 Brisbourne, A.M., Rydt, J., Graham, A.G., Spagnolo, M., 2017. Diverse landscapes beneath Pine Island
621 Glacier influence ice flow. Nature communications 8, 1618.

622 Boulton, G.S., 1996. Theory of glacial erosion, transport and deposition as a consequence of
623 subglacial deformation. Journal of Glaciology 42, 43-62.

624 Boulton, G.S., Hindmarsh, R.C.A., 1987. Sediment deformation beneath glaciers: rheology and
625 geological consequences. Journal of Geophysical Research 92, 9059-9082.

626 Boulton, G.S., Dobbie, K.E., Zatsepin, S., 2001. Sediment deformation beneath glaciers and its
627 coupling to the subglacial hydraulic system. Quaternary International 86, 3-28.

628 Boyce, J.I., Eyles, N., 2000. Architectural element analysis applied to glacial deposits: internal
629 geometry of a late Pleistocene till sheet, Ontario, Canada. Bulletin of the Geological Society of
630 America 112, 98-118.

631 Brumme, J., 2015. Three-dimensional microfabric analyses of Pleistocene tills from the cliff section
632 Dwasieden on Rügen (Baltic Sea coast): micromorphological evidence for subglacial polyphase
633 deformation (PhD thesis). Ernst-Moritz-Arndt-Universitstäat, Greifswald, 210pp.

634 Clarke, G.K.C., 1987. Subglacial till: a physical framework for its properties and processes. Journal of
635 Geophysical Research 92, 9023-9036.

636 Cuffey, K.M., Paterson, W.S.B., 2010. The Physics of Glaciers Fourth Edition. Academic Press, Oxford.

637 Denis, M., Guiraud, M., Konaté, M., Buoncristiani, J.-F., 2010. Subglacial deformation and water-
638 pressure cycles as a key for understanding ice stream dynamics: evidence from the Late Ordovician
639 succession of the Djado Basin (Niger). International Journal of Earth Science (Geol Rundsch) 99,
640 1399-1425.

641 Dyke, A.S., Morris, T.F., 1988. Drumlin fields, dispersal trains, and ice streams in Arctic Canada.
642 Canadian Geographer 32, 86–90.

643 Evans, D.J., Phillips, E.R., Hiemstra, J.F., Auton, C.A., 2006. Subglacial till: formation, sedimentary
644 characteristics and classification. Earth Science Reviews 78, 115-176.

645 Evans, D.J.A., Roberts, D.H., Evans, S.C., 2016. Multiple subglacial till deposition: A modern exemplar

646 for Quaternary palaeoglaciology. Quaternary Science Reviews 145, 183-203.

647 Evans, D.J.A., 2018. Till: A Glacial Process Sedimentology. John Wiley and Sons Ltd, UK.

648 Fairchild, I.J., Bradby, L., Spiro, B., 1993. Carbonate diagenesis in ice. Geology 21, 901-904.

649 Fairchild, I.J., Bradby, L., Spiro, B., 1994. Reactive carbonate in glacial systems: a preliminary

650 synthesis of its creation, dissolution and reincarnation. In Deymoux, M., Miller, J.M.G., Domack,

651 E.W., Young, G.M. (Eds) International Geological Correlation Project 260: Earth's Glacial record.

652 Cambridge University Press. 176-192.

653 Fuller, S., Murray, T., 2002. Sedimentological investigations in the forefield of an Icelandic surge-type

654 glacier: implications for the surge mechanism. Quaternary Science Reviews 21, 1503-1520.

655 Gehrmann, A., Hüneke, H., Meschede, M., Phillips, E. 2017. 3D microstructural architecture of

656 deformed glacigenic sediments associated with large-scale glacitectonism, Jasmund Peninsula (NE

657 Rügen), Germany. Journal of Quaternary Science 32, 213-230. DOI: 10.1002/jqs.2843.

658 Hart, J.K., Boulton, G.S., 1991. The interrelation of glaciotectonic and glaciodepositional processes

659 within the glacial environment. Quaternary Science Reviews 10, 335-350.

660 Hiemstra, J.F., van der Meer, J.J.M., 1997. Pore-water controlled grain fracturing as an indicator for

661 subglacial shearing in tills. Journal of Glaciology 43, 446-454.

662 Hiemstra, J.F., Rijsdijk, K.F. 2003. Observing artificially induced strain: implications for subglacial

663 deformation. Journal of Quaternary Science 18, 373-383.

664 Hiemstra, J.F., Rijsdijk, K.F., Evans, D.J.A., van der Meer, J.J.M., 2005. Integrated micro- and macro-

665 scale analyses of Last Glacial maximum Irish Sea diamicts from Abermaw and Treath y Mwnt, Wales,

666 UK. Boreas 34, 61-74.

667 Hindmarsh, R.C.A., 1998b. The stability of a viscous till sheet coupled with ice flow, considered at

668 wavelengths less than the ice thickness. Journal of Glaciology 44, 285-292.

669 Hindmarsh, R.C., 2009. Consistent generation of ice-streams via thermo-viscous instabilities

670 modulated by membrane stresses. Geophysical Research Letters 36(6).

671 Hodgson, D.A., 1994. Episodic ice streams and ice shelves during retreat of the northwestern most

672 sector of the Late Wisconsinan Laurentide Ice Sheet over the central Canadian Arctic archipelago.

673 Boreas 23, 14-28.

674   Humphrey, N., Kamb, B., Fahnestock, M., Engelhardt, H., 1993. Characteristics of the bed of the
675   lower Columbia Glacier, Alaska. Journal of Geophysical Research 98, 837-846.

676   Iverson, N.R., 2011. Shear resistance and continuity of subglacial till: hydrology rules. Journal of
677   Glaciology 56, 1104-1114.

678   Iverson, N.R., Hooyer, T.S., Baker, R.W. 1998. Ring-shear studies of till deformation: Coulomb-plastic
679   behaviour and distributed strain in glacier beds. Journal of Glaciology 44, 634-642.

680   Johnson, S.E. 1990. Lack of porphyroblast rotation in the Otago schists. New Zealand: implications
681   for crenulation cleavage development, folding and deformation partitioning. Journal of
682   Metamorphic Geology 8, 13-30.

683   King, E.C., Hindmarsh, R.C., Stokes, C.R., 2009. Formation of mega-scale glacial lineations observed
684   beneath a West Antarctic. Nature Geoscience 2, 585–588.

685   Kjaer, K.H., Houmark-Nielsen, M., Richardt, N., 2003. Ice-flow patterns and dispersal of erratics at
686   the southwestern margin of the last Scandinavian Ice Sheet: signature of palaeo-ice streams. Boreas
687   32, 130-148.

688   Kjær, K.H., Larsen, E., van der Meer, J.J.M., Ingólfsson, Ó., Krüger, J., Benediktsson, I.Ó., Knudsen,
689   C.G., Schomacker, A., 2006. Subglacial decoupling at the sediment/bedrock interface: a new
690   mechanism for rapid flowing ice. Quaternary Science Reviews 25, 2704-2712.

691   Khatwa, A., Tulaczyk, S., 2001. Microstructural interpretations of modern and Pleistocene
692   subglacially deformed sediments: the relative role of parent material and subglacial processes.
693   Journal of Quaternary Science 16, 507-517.

694   Kozarski, S., 1988. Time and dynamics of the last Scandinavian ice-sheet retreat from northwestern
695   Poland. Geographica Polonica 55, 91-101.

696   Kyrke-Smith, T.M., Katz, R.F., Fowler, A.C., 2015. Subglacial hydrology as a control on emergence,
697   scale, and spacing of ice streams. Journal of Geophysical Research: Earth Surface 120, 1501-1514.

698   Lachniet, M.S., Larson, G.J., Lawson, D.E., Evenson, E.B., Alley, R.B., 2001. Microstructures of
699   sediment flow deposits and subglacial sediments: a comparison. Boreas 30, 254-262.

700   Larsen, N. K., Piotrowski, J. A. and Kronborg, C. 2004. A multiproxy study of a basal till: a time-
701   transgressive accretion and deformation hypothesis. Journal of Quaternary Science 19, 9–21

702 Larsen, N.K., Piotrowski, J.A., Christiansen, F., 2006. Microstructures and micro-shears as proxy for

703 strain in subglacial diamicts: implications for basal till formation. Geology. 34, 889-892.

704 Larsen, N.K., Piotrowski, J.A., Menzies, J., 2007. Microstructural evidence of low-strain, time

705 transgressive subglacial deformation. Journal of Quaternary Science. 22, 593-608.

706 Lea, J.M., Palmer, A., 2014. Quantification of turbate microstructures through a subglacial till:

707 dimensions and characteristics. Boreas. 10.1111/bor.12073. ISSN 0300-9483.

708 Lee, J.R., Phillips, E.R., 2008. Progressive soft sediment deformation within a subglacial shear zone –

709 a hybrid mosaic-pervasive deformation model for Middle Pleistocene glaciotectonised sediments

710 from eastern England. Quaternary Science Reviews 27, 1350-1362.

711 Leighton, I.D., Hiemstra, J.F., Weidman, C.T., 2012. Recognition of micro-scale deformation

712 structures in glacial sediments – pattern perception, observer bias and the influence of experience.

713 Boreas, 10.1111/j.1502-3885.2011.00246.x. ISSN 0300-9483.

714 McGillen, M.R., Fairchild, I.J., 2005. An experimental study of incongruent dissolution of $CaCO_3$ under

715 analogue glacial conditions. Journal of Glaciology 51, 383-390.

716 Marks, L., 2012. Timing of the Late Vistulian (Weichselian) glacial phases in Poland. Quaternary

717 Science Reviews 44, 81-88.

718 Margold, M., Stokes, C.R., Clark, C.D. 2015. Ice Streams in the Laurentide Ice Sheet: Identification,

719 characteristics and comparison to modern ice sheets. Earth-Science Reviews 143, 117-146.

720 Menzies, J., 1982. Till hummock (proto-drumlin) at the ice glacier bed interface. In: Davidson-Arnott,

721 R., Nickling, W., Fahey, B.D. (Eds.), Research in Glacial, Glacio-Fluvial and Glacio-Lacustrine Systems.

722 Proceedings of the 6th Guelph Symposium on Geomorphology, 33-47.

723 Menzies, J., 2000. Micromorphological analyses of microfabrics and microstructures indicative of

724 deformation processes in glacial sediments. In: A.J. Maltman, B. Hubbard, M.J. Hambrey (eds.).

725 Deformation of glacial materials. Geological Society of London, Special Publication 176, 245-257.

726 Menzies, J., 2012. Strain pathways, till internal architecture and microstructures – perspectives on a

727 general kinematic model – a 'blueprint' for till development. Quaternary Science Reviews 50, 105-

728 124.

729 Menzies, J., Maltman, A.J., 1992. Microstructures in diamictons - evidence of subglacial bed

730 conditions. Geomorphology 6, 27-40.

731   Menzies, J., Brand, U., 2007. The internal sediment architecture of a drumlin, Port Byron, New York

732   State, USA. Quaternary Science Reviews 26, 322-335.

733   Menzies, J., Zaniewski, K., Dreger, D., 1997. Evidence from microstructures of deformable bed

734   conditions within drumlins, Chimney Bluffs, New York State. Sedimentary Geology 111, 161-175.

735   Menzies, J., van der Meer, J.J.M., Rose, J., 2006. Till – a glacial "tectomict", a microscopic

736   examination of a till's internal architecture. Geomorphology 75, 172-200.

737   Menzies, J., Hess, D.P., Rice, J.M., Wagner, K.G., Ravier, E., 2016. A case study in the New York

738   Drumlin Field, an investigation using microsedimentology, resulting in the refinement of a theory of

739   drumlin formation. Sedimentary Geology 338, 84-96.

740   Meriano, M., Eyles, N., 2009. Quantitative assessment of the hydraulic role of subglaciofluvial

741   interbeds in promoting deposition of deformation till (Northern Till, Ontario). Quaternary Science

742   Reviews 28, 608-620.

743   Narloch, W., Piotrowski, J.A., Wysota, W., Larsen, N.K., Menzies, J., 2012. The signature of strain

744   magnitude in tills associated with the Vistula Ice Stream of the Scandinavian Ice Sheet, central

745   Poland. Quaternary Science Reviews 57, 105-120.

746   Narloch, W., Wysota, W., Piotrowski, J.A., 2013. Sedimentological record of subglacial conditions and

747   ice sheet dynamics of the Vistula Ice Stream (north-central Poland) during the Last Glaciation.

748   Sedimentary Geology 293, 30-44.

749   Neudorf, C. M., Brennand, T. A., Lian, O. B., 2013. Till-forming processes beneath parts of the

750   Cordilleran Ice Sheet, British Columbia, Canada: macroscale and microscale evidence and a new

751   statistical technique for analysing microstructure data. Boreas, 10.1111/bor.12009. ISSN 0300-9483.

752   O´Cofaigh, C., Evans, J., Dowdeswell, J.A., Larter, R. 2007. Till characteristics, genesis and transport

753   beneath Antarctic paleo-ice streams. Journal of Geophysical Research 112, F03006.

754   Palmer, A.P. 2005. The micromorphological description, interpretation and palaeoenvironmental

755   significance of lacustrine clastic laminated sediments. Unpublished PhD thesis, University of London.

756   Passchier, C.W., Trouw, R.A.J., 1996. Microtectonics. Springer.

757   Patterson, C.J., 1997. Southern Laurentide ice lobes were created by ice streams: Des Moines Lobe in

758   Minnesota, USA. Sedimentary Geology 111, 249-261.

759   Patterson, C.J., 1998. Laurentide glacial landscapes: the role of ice streams. Geology 26, 643-646.

Phillips, E.R., 2006. Micromorphology of a debris flow deposit: evidence of basal shearing, hydrofracturing, liquefaction and rotational deformation during emplacement. Quaternary Science Reviews 25, 720-738.

Phillips, E., Merritt, J.W., Auton, C.A., Golledge, N.R., 2007. Microstructures developed in subglacially and proglacially deformed sediments: faults, folds and fabrics, and the influence of water on the style of deformation. Quaternary Science Reviews 26, 1499-1528.

Phillips, E.R., Auton, C.A., 2000. Micromorphological evidence for polyphase deformation of glaciolacustrine sediments from Strathspey, Scotland. In: Maltman, A.J., Hubbard, B., Hambrey, M.J. (Eds). Deformation of glacial materials. The Geological Society of London, Special Publication 176, 279-291.

Phillips, E.R., Auton, C.A., 2008. Microtextural analysis of a glacially 'deformed' bedrock: implications for inheritance of preferred clast orientations in diamictons. Journal of Quaternary Science 23, 229-240.

Phillips, E., Merritt, J., 2008. Evidence for multiphase water-escape during rafting of shelly marine sediments at Clava, Inverness-shire, NE Scotland. Quaternary Science Reviews 27, 988–1011.

Phillips, E.R., van der Meer, J.J.M., Ferguson, A., 2011. A new 'microstructural mapping' methodology for the identification and analysis of microfabrics within glacial sediments. Quaternary Science Reviews 30, 2570-2596.

Phillips, E., Everest, J., Reeves, H., 2013. Micromorphological evidence for subglacial multiphase sedimentation and deformation during overpressurized fluid flow associated with hydrofracturing. Boreas 42, 395–427.

Phillips, E.R., Lipka, E., van der Meer, J.J.M. 2013. Micromorphological evidence of liquefaction and sediment deposition during basal sliding of glaciers. Quaternary Science Reviews 81, 114-137.

Phillips, E., Evans, D.J.A., van der Meer, J.J.M., Lee, J.R. 2018. Microscale evidence of liquefaction and its potential triggers during soft-bed deformation within subglacial traction tills. Quaternary Science Reviews 181, 123-143.

Piotrowski, J.A., 1994a. In Warren, W.P., Croot, D. (eds) Formation and Deformation of Glacial Deposits, Balkema, Rotterdam. 3-8.

788   Piotrowski, J.A., 1994b. Tunnel-valley formation in northwest Germany—geology, mechanisms of
789   formation and subglacial bed conditions for the Bornhöved Tunnel Valley. Sedimentary Geology 89,
790   107-141.

791   Piotrowski, J.A., Kraus, A.M., 1997. Response of sediment to ice sheet loading in northwestern
792   Germany: effective stresses and glacier bed stability. Journal of Glaciology 43, 495-502.

793   Piotrowski, J.A., Tulaczyk, S., 1999. Subglacial conditions under the last ice sheet in northwest
794   Germany: ice-bed separation and enhanced basal sliding? Quaternary Science Reviews 18, 737-751.

795   Piotrowski, J.A., Mickelson, D.M., Tulaczyk, S., Krzyszowski, D., Junge, F. 2001. Were subglacial
796   deforming beds beneath past ice sheets really widespread? Quaternary International 86, 139-150.

797   Piotrowski, J.A., Larsen, N.K., Junge, F., 2004. Soft subglacial beds: a mosaic of deforming and stable
798   spots. Quaternary Science Reviews 23, 993-1000.

799   Piotrowski, J.A., Larsen, N.K., Menzies, J., Wysota, W., 2006. Formation of subglacial till under
800   transient bed conditions: deposition, deformation, and basal decoupling under a Weichselian ice
801   sheet lobe, central Poland. Sedimentology 53, 83-106.

802   Przybylski, B., 2008. Geomorphic traces of a Weichselian ice stream in the Wielkopolska Lowland,
803   western Poland. Boreas 37, 286-296.

804   Spagnolo, M., Clark, C.D., Ely, J.C., Stokes, C.R., Anderson, J.B., Andreassen, K., Graham, A.G.C., King,
805   E.C., 2014. Size, shape and spatial arrangement of mega-scale glacial lineations. Earth Surface
806   Processes and Landforms 39, 1432-1448.

807   Spagnolo, M., Phillips, E., Piotrowski, J.A., Rea, B.R., Clark, C.D., Stokes, C.R., Carr, S.J., Ely, J.C.,
808   Adriano Ribolini, A., Wysota, W., Izabela Szuman, I., 2016. Ice stream motion facilitated by a shallow-
809   deforming and accreting bed. Nature Communications DOI: 10.1038/ncomms10723.

810   Spagnolo, M., Bartholomaus, T.C., Clark, C.D., Stokes, C.R., Atkinson, N., Dowdeswell, J.A., Ely, J.C.,
811   Graham, A., Hogan, K.A., King, Larter, R.D., E., Livingstone, S.J., Pritchard. H.D., 2017. The periodic
812   topography of ice stream beds: insights from the Fourier spectra of mega-scale glacial lineations.
813   Journal of Geophysical Research: Earth Surface 122, 1355-1373.

814   Stokes, C.R., Clark, C.D., 1999. Geomorphological criteria for identifying Pleistocene ice streams.
815   Annals of Glaciology 28, 67-75.

816   Stokes, C.R., Clark, C.D., 2001. Palaeo-ice streams. Quaternary Science Reviews 20, 1437-1457.

817   Stokes, C.R., Clark, C.D., 2002. Are long subglacial bedforms indicative of fast ice flow? Boreas 31,
818   239-249.

819   Stokes, C.R., Clark, C.D., 2003. The Dubawnt Lake palaeo-ice stream: evidence for dynamic ice sheet
820   behaviour on the Canadian Shield and insights regarding the controls on ice stream location and
821   vigour. Boreas 32, 263-279.

822   Stokes, C.R., Fowler, A.C., Clark, C.D., Hindmarsh, R.C.A., Spagnolo, M., 2013a. The instability theory
823   of drumlin formation and its explanation of their varied composition and internal structure.
824   Quaternary Science Reviews 62, 77–96.

825   Stokes, C.R., Spagnolo, M., Clark, C.D., Ó Cofaigh, C., Lian, O.B., Dunstone, R.B., 2013b. Formation of
826   mega-scale glacial lineations on the Dubawnt Lake Ice Stream bed: 1. Size, shape and spacing from a
827   large remote sensing dataset. Quaternary Science Reviews 77, 190–209.

828   Thomason, J.F., Iverson, N.R., 2006 Microfabric and micro-shear evolution in deformed till.
829   Quaternary Science Reviews 25, 1027-1038.

830   Truffer, M., Harrison, W.D., Echelmeyer, K.A., 2000. Glacier motion dominated by processes deep in
831   underlying till. Journal of Glaciology 46, 213e221. https://doi.org/10.3189/172756500781832909.

832   Tulaczyk, S., 1999 Ice sliding over weak, fine-grained tills: dependence of ice-till interactions on till
833   granulometry. Special Papers Geological Society of America 337, 159-177.

834   Tulaczyk, S., Kamb, B., Scherer, R.P., Engelhardt, H.F., 1998. Sedimentary processes at the base of a
835   West Antarctic ice stream: constraints from textural and compositional properties of subglacial
836   debris. Journal of Sedimentary Research 68, 487-496.

837   van der Meer, J.J.M., 1987. Micromorphology of glacial sediments as a tool in distinguishing genetic
838   varieties of till. Geological Survey of Finland Special Paper 3, 77-89.

839   van der Meer, J.J.M., 1993. Microscopic evidence of subglacial deformation. Quaternary Science
840   Reviews 12, 553-587.

841   van der Meer, J.J.M., 1997. Particle and aggregate mobility in till: microscopic evidence of subglacial
842   processes. Quaternary Science Reviews 16, 827-831.

843   van der Meer, J.J.M., Menzies, J., Rose, J., 2003. Subglacial till, the deformable glacier bed.
844   Quaternary Science Reviews 22, 1659-1685.

845 van der Meer, J.J.M., Kjær, K.H., Krüger, J., Rabassa, J., Kilfeather, A.A., 2009. Under pressure: clastic

846 dykes in glacial settings. Quaternary Science Reviews 28, 708-720.

847 van der Wateren, F.M., Kluiving, S.J., Bartek, L.R., 2000. Kinematic indicators of subglacial shearing.

848 In: A.J. Maltman, B. Hubbard, M.J. Hambrey (eds.) Deformation of glacial materials. Geological

849 Society of London, Special Publication. 176, 259-278.

850 Vaughan-Hirsch, D.P., Phillips, E., Lee, J.R., Hart, J.K., 2013. Micromorphological analysis of poly-

851 phase deformation associated with the transport and emplacement of glaciotectonic rafts at West

852 Runton, north Norfolk, UK. Boreas 42, 376–394.

853 Vernon, R.H., 1989. Porphyroblast-matrix microstructural relationships: recent approaches and

854 problems. In Daly et al. (Eds), Evolution of metamorphic belts. Geological Society of London, Special

855 Publication 43, 83-102.

856

10. Figures

858 **Fig. 1. (a)** and **(b)** Maps showing the location of the study area in western Poland; **(c)** Digital

859 Elevation Model (DEM) of the Środa Wielkopolska area showing the well-developed NW-SE-trending

860 megascale glacial lineations and locations of the trenches excavated into these subglacial landforms.

861 Also shown is the SE-directed regional ice flow across the area; and **(d)** An example of a trench dug

862 into the Quaternary sediments forming the landforms showing the position of the samples collected

863 for thin sectioning. Note that the samples were collected from below the base of the soil layer.

864 **Fig. 2.** Microstructural map and high resolution scan of thin section C1M. The orientation of the long

865 axes of sand to granule sized clasts included within the diamicton are shown on a series of rose

866 diagrams. The thin section has been subdivided into 16 subareas and the E1 and E2 eigenvalues

867 calculated for each area (see text for details).

868 **Fig. 3.** Microstructural map and high resolution scan of thin section C2M. The orientation of the long

869 axes of sand to granule sized clasts included within the diamicton are shown on a series of rose

870 diagrams. The thin section has been subdivided into 16 subareas and the E1 and E2 eigenvalues

871 calculated for each area (see text for details).

872 **Fig. 4.** Microstructural map and high resolution scan of thin section C3M. The orientation of the long

873 axes of sand to granule sized clasts included within the diamicton are shown on a series of rose

874 diagrams. The thin section has been subdivided into 16 subareas and the E1 and E2 eigenvalues

875 calculated for each area (see text for details).

876 **Fig. 5.** Microstructural map and high resolution scan of thin section C4M. The orientation of the long

877 axes of sand to granule sized clasts included within the diamicton are shown on a series of rose

878 diagrams. The thin section has been subdivided into 16 subareas and the E1 and E2 eigenvalues

879 calculated for each area (see text for details).

880 **Fig. 6.** Microstructural map and high resolution scan of thin section C5M. The orientation of the long

881 axes of sand to granule sized clasts included within the diamicton are shown on a series of rose

882 diagrams. The thin section has been subdivided into 16 subareas and the E1 and E2 eigenvalues

883 calculated for each area (see text for details).

884 **Fig. 7.** Microstructural map and high resolution scan of thin section C6M. The orientation of the long

885 axes of sand to granule sized clasts included within the diamicton are shown on a series of rose

886 diagrams. The thin section has been subdivided into 16 subareas and the E1 and E2 eigenvalues

887 calculated for each area (see text for details).

888 **Fig. 8.** Microstructural maps and automated clast density maps of the main clast microfabrics (S2, S3,

889 S4, S5) identified within samples X1M, Y1M and Z1M.

890 **Fig. 9.** Photomicrographs showing the fine-grained, dusty looking carbonate which locally replaces

891 the matrix to the diamicton (**a** to **c**) and clay lined and filled pore spaces (**d** to **f**).

892 **Fig. 10. (a)** Diagram showing the relationships between the different sets of Riedel shears developed

893 within the diamicton in response to deformation imposed by the overriding ice stream; and **(b)**

894 Example of a detailed microstructural map of sample C1M. The coloured polygons represent the

895 different generations of clast microfabrics, which define the Riedel shears, subhorizontal shear fabric

896 and up-ice dipping foliation.

897 **Fig. 11.** Graphs showing the effects of grain size on clast microfabric development within the

898 diamicton at site C. The long axis data for each thin section (C1M to C6M) are divided into three sets:

899 (i) grains < 0.25 mm in length; (ii) grains between 0.25 to 0.5 mm in size; and (iii) grains over > 0.5

900 mm in length. The number of grains in each of the three classes is plotted against the orientation of

901 their long axis (0° represents horizontal). The large "spike" in the data set for the finest grains and

902 total clasts at 0° results from the unavoidable "snapping" to the horizontal of short long axes dipping

903 at very low angles (-2° to +2°) during digitisation using CorelDraw. On Figure 12 the data are plotted

904 on a series of rose diagrams showing the dip of the long axes within the 2D plane of the thin section.

Fig. 12. Rose diagrams showing the variation in dip of the long axes of coarse silt to sand sized clasts within the 2D plane of the thin sections C1M to C6M. The data are divided into three sets: (i) grains < 0.25mm in length; (ii) grains between 0.25 to 0.5 mm in size; and (iii) grains over > 0.5 mm in length.

Fig. 13. Variation in E1 eigenvalues calculated for the thin sections (C1M to C6M) showing the variation is relative fabric strength both with an individual thin section and vertically through the diamicton at site C. Red colours represents areas of the thin sections with higher E1 values (0.65-0.68) and purple low E1 values (0.53-0.51).

Fig. 14. (a) Plot showing the variation in average E1 eigenvalue calculated for each thin section (C1M to C6M) with respect to depth within the diamicton sequence; and **(b)** Plot of E1 eigenvalue against shear strain. The shear strain curves for the Batestown (gravelly) and Douglas (sand-rich) tills are taken from Thomason and Iverson (2006) and are used to obtain an estimate of the range of shear strains encountered by the diamicton exposed at site C.

Fig. 15. Diagram showing the variation in clast microfabric development at site C.

Fig. 16. (a) Cartoon showing the passive rotation of elongate clasts into the plane of the developing microfabric. Further deformation of clasts aligned within this fabric is thought to occur in response to grain sliding; **(b)** Strain field diagram modified from Bell *et al*. (1986) used here to show the proposed geometry of the strain field formed in response to the presence of large immobile clasts within a weaker deforming matrix; and **(c)** Schematic diagram showing the development of anastomosing clast microfabrics within a till defined by the preferred shape alignment of finer grained clasts. The spacing of the microfabric domains is controlled by the grain size and spacing of the larger sand to pebble sized clasts in response to deformation partitioning within the till.

Fig. 17. Schematic profiles through the bed of a glacier and the resulting idealised cumulative strain curves: **(a)** Pervasive deformation throughout the subglacial shear zone with the amount of strain increasing upwards towards the ice-bed interface; **(b)** Deformation partitioning within the subglacial shear zone with localised detachments forming at deeper levels within the bed; and **(c)** Deformation confined to the "active" layer located at the top of the bed with shearing migrating upwards keeping pace with till accretion (cf. Larsen *et al*., 2004).

11. Tables

Table 1. Detrital clast assemblage identified within the silty sand subglacial traction till exposed at Site C.

Sample Number	Detrital Components	
	major	*minor to accessory*
C1M	monocrystalline quartz, feldspar (plagioclase, K-feldspar)	polycrystalline quartz, opaque minerals, altered volcanic rocks, clinopyroxene, microcline, mudstone, sericitised granitic rock, amphibole, glauconitic material, micrographic intergrowth, ?alkali granite, garnet
C2M	monocrystalline quartz, feldspar (plagioclase, K-feldspar)	cryptocrystalline quartz (chert), opaque minerals, pyroxene, siltstone, mudstone, microcline, altered igneous rock, glauconitic material, micrographic intergrowth, amphibole, feldspar-chlorite rock, biotite-schistose metamorphic rock, fine sandstone (hematitic cement)
C3M	monocrystalline quartz	polycrystalline quartz, biotite, metamorphic rock, indurated quartz-arenite, echinoderm fragments, plagioclase, carbonate mineral(s), micritic limestone, brachiopod fragments, K-feldspar, glauconitic material, amphibole, opaque minerals, cryptocrystalline quartz (chert), very fine-grained micaceous material, epidote, siltstone/very fine-grained sandstone, foraminifera, garnet, ?zircon, muscovite
C4M	monocrystalline quartz, feldspar (plagioclase, K-feldspar)	micrographic intergrowth, carbonate minerals, mudstone, microcline, glauconitic material, amphibole, indurated siltstone, bioclastic limestone, glauconite-bearing micritic limestone, biotite, ?alkali granitic rock, micritic limestone, hematised siltstone, opaque minerals, altered granitic rock, ?garnet, brachiopod fragments, echinoderm fragments, quartz-epidote-rock, amphibolite
C5M	monocrystalline quartz	polycrystalline quartz, siltstone, amphibole, opaque minerals, carbonate minerals, micritic limestone, glauconitic material, microcline, plagioclase, altered granitic rock, devitrified igneous rock/felsite, zircon, muscovite, garnet, bioclastic limestone, glauconitic sandstone, biotite metamorphic rock
C6M	monocrystalline quartz	plagioclase, K-feldspar, carbonate minerals, bioclastic limestone, glauconitic material, micritic bioclastic limestone, muscovite-granite, amphibole, opaque minerals, biotite-granite, laminated siltstone, amphibolite, altered igneous rock, microcline, garnet, calcareous siltstone, very fine-grained sandstone/siltstone, zircon, epidote, tourmaline

Table 2. Average E1 and E2 eigenvalues calculated for clast microfabrics developed within subglacial traction till samples C1M to C6M.

Depth below surface (cm)	Sample	Eigenvalues									
		E1	E1	E1	E1	E1	E1	E1	E1	Median	Average
21	C1M a-h	0.555	0.582	0.578	0.580	0.582	0.573	0.570	0.549	0.575	0.571
24	C1M i-p	0.604	0.575	0.591	0.601	0.561	0.605	0.576	0.571	0.584	0.586
46	C2M a-h	0.583	0.588	0.589	0.631	0.600	0.565	0.606	0.562	0.588	0.590
49	C2M i-p	0.579	0.594	0.588	0.562	0.582	0.584	0.597	0.580	0.583	0.583
71	C3M a-h	0.649	0.642	0.618	0.635	0.654	0.658	0.651	0.629	0.646	0.642
74	C3M i-p	0.638	0.640	0.645	0.626	0.596	0.617	0.600	0.627	0.627	0.624
96	C4M a-h	0.559	0.540	0.523	0.550	0.564	0.561	0.553	0.586	0.556	0.555
99	C4M i-p	0.545	0.552	0.530	0.517	0.547	0.531	0.542	0.560	0.544	0.541
121	C5M a-h	0.521	0.566	0.541	0.528	0.557	0.554	0.557	0.571	0.555	0.549
124	C5M i-p	0.526	0.552	0.562	0.571	0.559	0.556	0.573	0.613	0.561	0.564
146	C6M a-h	0.573	0.556	0.534	0.571	0.568	0.551	0.568	0.582	0.568	0.563
154	C6M i-p	0.556	0.566	0.561	0.569	0.542	0.535	0.530	0.570	0.559	0.554
		E2	E2	E2	E2	E2	E2	E2	E2	Median	Average
21	C1M a-h	0.444	0.417	0.421	0.419	0.417	0.426	0.429	0.450	0.424	0.428
24	C1M i-p	0.395	0.424	0.408	0.398	0.438	0.394	0.423	0.428	0.415	0.413
46	C2M a-h	0.416	0.411	0.410	0.368	0.399	0.434	0.393	0.437	0.411	0.409
49	C2M i-p	0.420	0.405	0.411	0.437	0.417	0.415	0.402	0.419	0.416	0.416

71	C3M a-h	0.350	0.357	0.381	0.364	0.345	0.341	0.348	0.370	0.353	0.357
74	C3M i-p	0.361	0.359	0.354	0.373	0.403	0.382	0.399	0.372	0.372	0.375
96	C4M a-h	0.440	0.459	0.476	0.449	0.435	0.438	0.446	0.413	0.443	0.444
99	C4M i-p	0.454	0.447	0.469	0.482	0.452	0.468	0.457	0.439	0.455	0.458
121	C5M a-h	0.478	0.43	0.458	0.471	0.442	0.445	0.442	0.428	0.444	0.450
124	C5M i-p	0.473	0.447	0.437	0.428	0.440	0.443	0.426	0.386	0.438	0.435
146	C6M a-h	0.426	0.443	0.465	0.428	0.431	0.448	0.431	0.417	0.431	0.436
154	C6M a-p	0.443	0.433	0.438	0.430	0.457	0.464	0.469	0.429	0.440	0.445

a

Norway
Sweden
Edinburgh
Denmark
Baltic Sea
Lithuania
UK
London
Poznan
Warsaw
Belarus
Germany
Poland
Ukraine
Czech Republic

b

Greater Poland

Pobiedziska
Poznan
Kostrzyn
Warsaw
Mosina
Sroda Wielkopolska
Srem
Jarocin
Leszno

N

20 km

c

640000   660000

Poznan

mega scale glacial lineations

D

C

Sroda
Wielkopolska

K-A-B   T-X-Y-Z

5790000

E

Ice Movement Direction

N

Elevation
133 m

56 m

0   2   4
km

△ trench

d

soil

sample 1

diamicton

sample 6

□ position of samples taken for thin sectioning
..... base of soil layer

orientation 122 degrees

scale = 10 mm

Sample C1M

orientation 122 degrees

Legend:
- S1 clast microfabric
- S2 clast microfabric
- S3 clast microfabric
- S4 clast microfabric
- subhorizontal Y-type Riedel shear
- moderately down-ce dipping R-type shears
- steeply down-ce dipping R'-type shears

- sense of shear
- orientation of clast long axis
- alignment of clast long axes
- clay lined fractures, voids and pore spaces

way up

moderately inclined down-ice dipping foliation (S4) defining extensional Riedel shears

moderately inclined, up-ice dipping foliation (S3) forming dominant fabric

subhorizontal foliation (S2) defining Y-type Riedel shears

early foliation (S1) deformed by small-scale crenulations

steeply inclined down-ice dipping R'-type Riedel shears

subhorizontal Y-type Riedel shears

clast microfabric domains defined by preferentially shape-aligned (long axes) detrital grains

scale = 10 mm

Sample C1M

down-ice dipping R-type Riedel shears

way up

Area B: N = 1179 — top

Area C: N = 1191 — top

Area D: N = 1133 — top

Area E: N = 1154 — top

Area F: N = 1083 — top

Area G: N = 1242 — top

Area A: N = 1192 — top

Area H: N = 967 — top

Area I: N = 577 — top

Area P: N = 745 — top

A	B	C	D	E	F	G	H
E1 = 0.5556 E2 = 0.4443	E1 = 0.5829 E2 = 0.4170	E1 = 0.5780 E2 = 0.4219	E1 = 0.5808 E2 = 0.4191	E1 = 0.5826 E2 = 0.4173	E1 = 0.5735 E2 = 0.4264	E1 = 0.5705 E2 = 0.4294	E1 = 0.5496 E2 = 0.4503

I	J	K	L	M	N	O	P
E1 = 0.6047 E2 = 0.3952	E1 = 0.5756 E2 = 0.4243	E1 = 0.5919 E2 = 0.4080	E1 = 0.6010 E2 = 0.3989	E1 = 0.5612 E2 = 0.4387	E1 = 0.6055 E2 = 0.3944	E1 = 0.5762 E2 = 0.4237	E1 = 0.5716 E2 = 0.4283

scale = 10 mm

Sample C1M

orientation 122 degrees

way up

Area J: N = 1099 — top

Area K: N = 1244 — top

Area L: N = 1064 — top

Area M: N = 1123 — top

Area N: N = 1003 — top

Area O: N = 1021 — top

orientation 122 degrees

scale = 10 mm

Sample C2M
orientation 122 degrees

Legend:
- S1 clast microfabric
- S2 clast microfabric
- S3 clast microfabric
- S4 clast microfabric
- S5 clast microfabric

- subhorizontal Y-type Riedel shear
- moderately down-ce dipping R-type shears
- steeply down-ce dipping R'-type shears
- subvertical anastomosing dewatering foliation

- sense of shear
- orientation of clast long axis
- alignment of clast long axes
- clay lined fractures, voids and pore spaces

moderately inclined down-ice dipping foliation (S4) defining extensional Riedel shears

moderately inclined, up-ice dipping foliation (S3) forming dominant fabric

subhorizontal foliation (S2) defining Y-type Riedel shears

early foliation (S1) deformed by small-scale crenulations

clast microfabric domians defined by preferentially shape-aligned (long axes) detrital grains

subhorizontal Y-type Riedel shears

subvertical anastomosing foliation (S5)

way up

scale = 10 mm

Sample C2M

down-ice dipping R-type Riedel shears

steeply inclined down-ice dipping R'-type Riedel shears

Area B: N = 1247
Area C: N = 1778
Area D: N = 1288
Area E: N = 1083
Area F: N = 1079
Area G: N = 1217
Area A: N = 840
Area H: N = 775
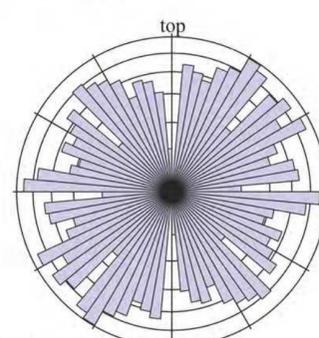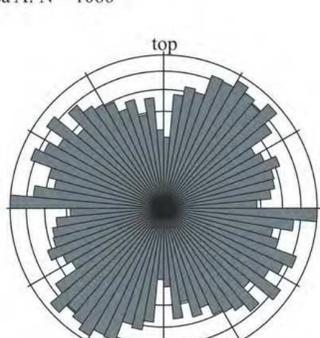Area I: N = 666
Area P: N = 1117
Area J: N = 1049
Area K: N = 1174
Area L: N = 1261
Area M: N = 1359
Area N: N = 1115
Area O: N = 1374

A	**B**	**C**	**D**	**E**	**F**	**G**	**H**
	E1 = 0.5838 E2 = 0.4161	E1 = 0.5882 E2 = 0.4117	E1 = 0.5891 E2 = 0.4108	E1 = 0.6319 E2 = 0.3680	E1 = 0.6002 E2 = 0.3997	E1 = 0.5653 E2 = 0.4346	E1 = 0.6060 E2 = 0.3939	E1 = 0.5627 E2 = 0.4372
I	**J**	**K**	**L**	**M**	**N**	**O**	**P**
E1 = 0.5795 E2 = 0.4204	E1 = 0.5945 E2 = 0.4054	E1 = 0.5881 E2 = 0.4118	E1 = 0.5625 E2 = 0.4374	E1 = 0.5825 E2 = 0.4174	E1 = 0.5849 E2 = 0.4150	E1 = 0.5971 E2 = 0.4028	E1 = 0.5801 E2 = 0.4198

scale = 10 mm

Sample C2M

orientation 122 degrees

way up

Sample C3M
orientation 122 degrees

Legend:
- S1 clast microfabric
- S2 clast microfabric
- S3 clast microfabric
- S4 clast microfabric
- S5 clast microfabric

- subhorizontal Y-type Riedel shear
- moderately down-ce dipping R-type shears
- steeply down-ce dipping R'-type shears
- subvertical anastomosing dewatering foliation
- micritic carbonate cement

→ sense of shear
/ orientation of clast long axis
/// alignment of clast long axes
/// clay lined fractures, voids and pore spaces

sinistral (down-ice) shear sense defined by S3 microfabric

subhorizontal Y-type Riedel shears

moderately inclined, up-ice dipping foliation (S3) forming dominant fabric

subhorizontal foliation (S2) defining Y-type Riedel shears

early foliation (S1) deformed by small-scale crenulations

subvertical anastomosing foliation (S5)

scale = 10 mm

Sample C3M
orientation 122 degrees

anastomosing zones of subvertical clast microfabric

moderately inclined down-ice dipping foliation (S4) defining extensional Riedel shears

down-ice dipping R-type Riedel shears

way up

Area A: N = 1433
Area B: N = 1724
Area C: N = 1654
Area D: N = 1647
Area E: N = 1540
Area F: N = 1380
Area G: N = 1510
Area H: N = 1233
Area I: N = 1173
Area J: N = 1428
Area K: N = 1265
Area L: N = 1250
Area M: N = 1146
Area N: N = 1069
Area O: N = 1132
Area P: N = 846

	A	B	C	D	E	F	G	H
E1	0.6499	0.6428	0.6189	0.6355	0.6545	0.6582	0.6512	0.6299
E2	0.3500	0.3571	0.3810	0.3644	0.3454	0.3417	0.3487	0.3700

	I	J	K	L	M	N	O	P
E1	0.6389	0.6408	0.6458	0.6263	0.5969	0.6178	0.6000	0.6278
E2	0.3610	0.3591	0.3541	0.3736	0.4030	0.3821	0.3999	0.3721

scale = 10 mm

Sample C3M
orientation 122 degrees

way up

Legend:
- S1 clast microfabric
- S2 clast microfabric
- S3 clast microfabric
- S4 clast microfabric
- S5 clast microfabric
- subhorizontal Y-type Riedel shear
- moderately down-ce dipping R-type shears
- steeply down-ce dipping R'-type shears
- subvertical anastomosing dewatering foliation
- micritic carbonate cement
- sense of shear
- orientation of clast long axis
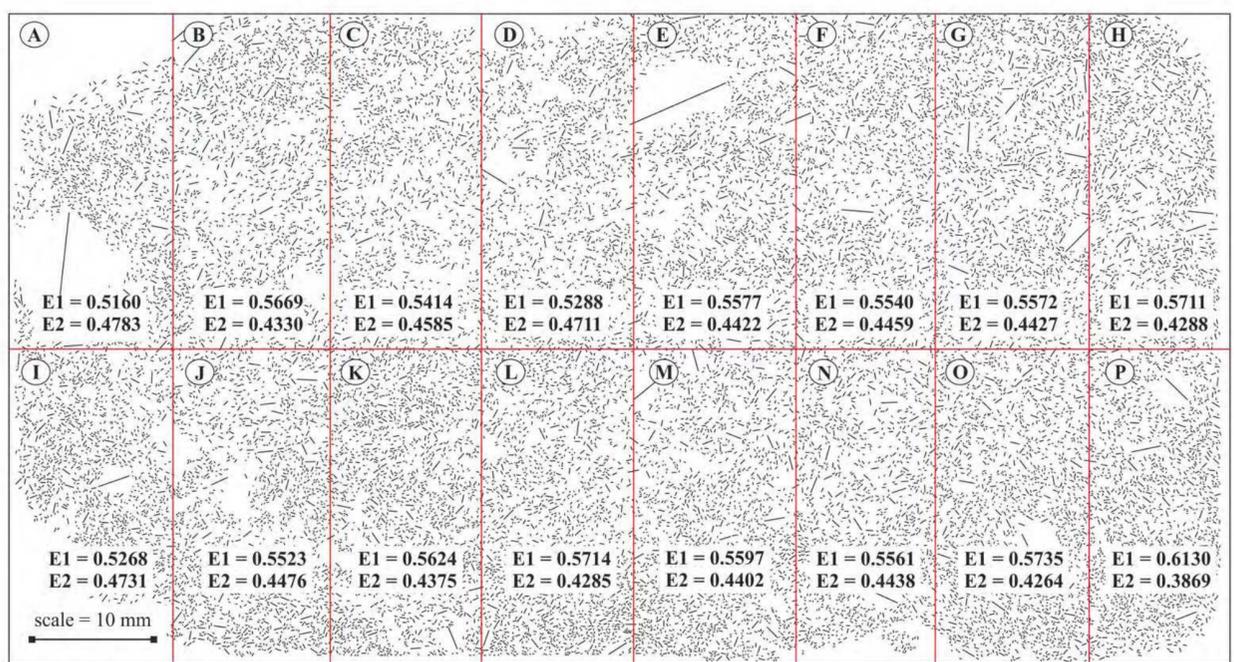- alignment of clast long axes
- clay lined fractures, voids and pore spaces

orientation 122 degrees

scale = 10 mm

Sample C4M
orientation 122 degrees

subhorizontal foliation (S2) defining Y-type Riedel shears

moderately inclined, up-ice dipping foliation (S3) forming dominant fabric

sinistral (down-ice) shear sense defined by asymmetrical microfabric

early foliation (S1) deformed by small-scale crenulations

subvertical anastomosing foliation (S5)

scale = 10 mm

way up

Sample C4M

anastomosing zones of subvertical clast microfabric (S5)

moderately inclined down-ice dipping foliation (S4) defining extensional Riedel shears

down-ice dipping R-type Riedel shears

Area B: N = 1335

Area C: N = 1218

Area D: N = 1165

Area E: N = 1427

Area F: N = 1204

Area G: N = 1409
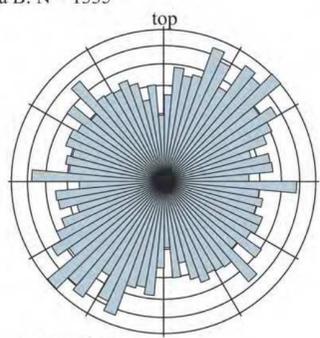
Area A: N = 1417

Area H: N = 1004

A	B	C	D	E	F	G	H
E1 = 0.5592 E2 = 0.4407	E1 = 0.5408 E2 = 0.4591	E1 = 0.5235 E2 = 0.4764	E1 = 0.5502 E2 = 0.4497	E1 = 0.5646 E2 = 0.4353	E1 = 0.5618 E2 = 0.4381	E1 = 0.5536 E2 = 0.4463	E1 = 0.5869 E2 = 0.4130

I	J	K	L	M	N	O	P
E1 = 0.5454 E2 = 0.4545	E1 = 0.5528 E2 = 0.4471	E1 = 0.5303 E2 = 0.4696	E1 = 0.5179 E2 = 0.4820	E1 = 0.5475 E2 = 0.4524	E1 = 0.5319 E2 = 0.4680	E1 = 0.5426 E2 = 0.4573	E1 = 0.5600 E2 = 0.4399

scale = 10 mm

Sample C4M

orientation 122 degrees

way up
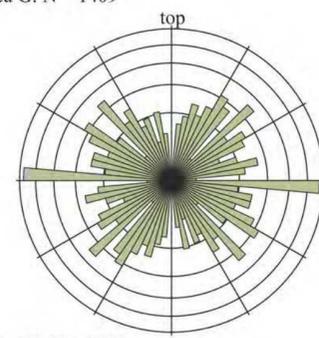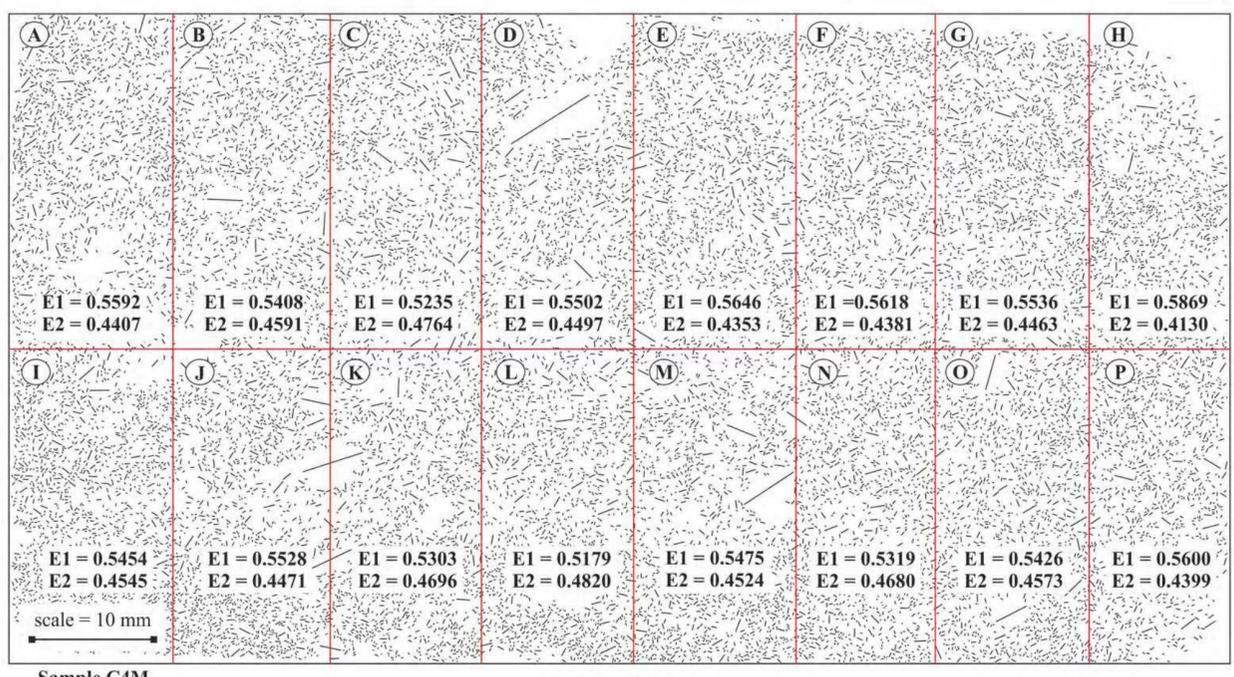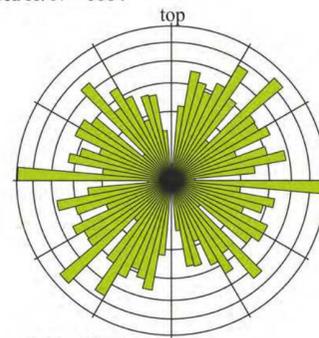
Area I: N = 1669

Area P: N = 1150
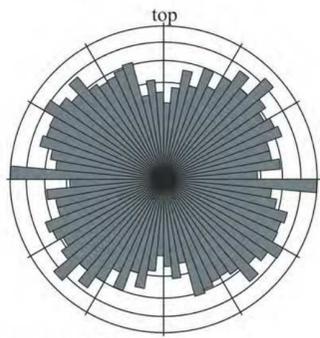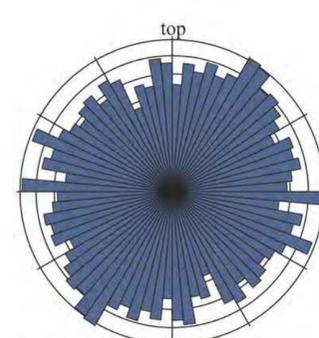
Area J: N = 1508

Area K: N = 1348
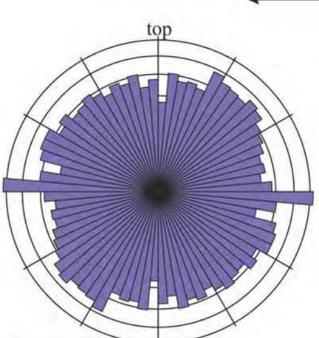
Area L: N = 1295
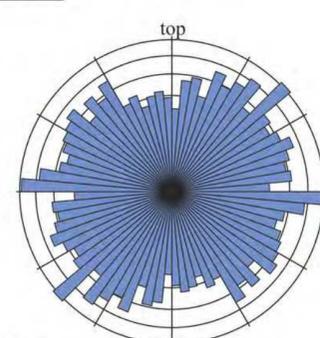
Area M: N = 1500

Area N: N = 1373

Area O: N = 1373

orientation 122 degrees

S1 clast microfabric
S2 clast microfabric
S3 clast microfabric
S4 clast microfabric
S5 clast microfabric

subhorizontal Y-type Riedel shear
moderately down-ce dipping R-type shears
steeply down-ce dipping R'-type shears
subvertical anastomosing dewatering foliation
micritic carbonate cement

sense of shear
orientation of clast long axis
alignment of clast long axes
clay lined fractures, voids and pore spaces

scale = 10 mm

way up

Sample C5M
orientation 122 degrees

subhorizontal foliation (S2) defining Y-type Riedel shears

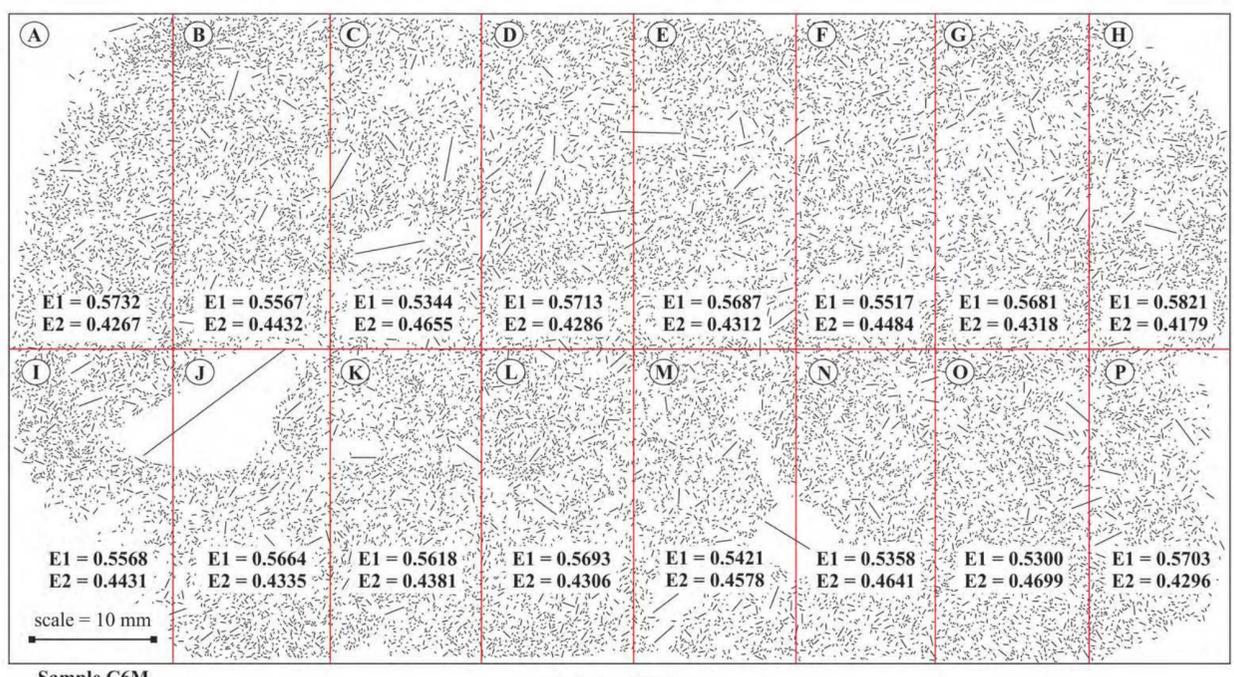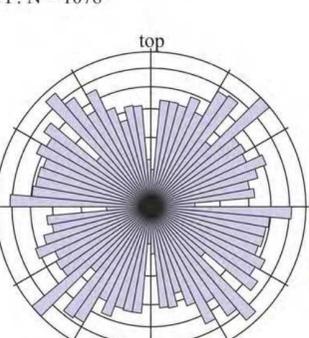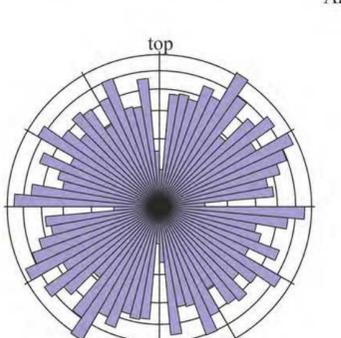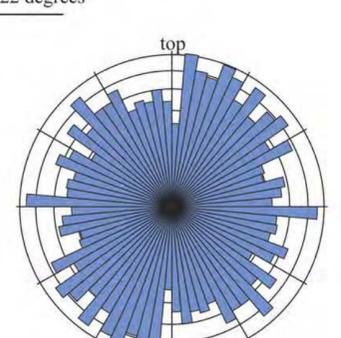moderately inclined, up-ice dipping foliation (S3) forming dominant fabric

sinistral (down-ice) shear sense defined by asymmetrical microfabric

early foliation (S1) deformed by small-scale crenulations

subvertical anastomosing foliation (S5)

scale = 10 mm

way up

Sample C5M

anastomosing zones of subvertical clast microfabric (S5)

moderately inclined down-ice dipping foliation (S4) defining extensional Riedel shears

down-ice dipping R-type Riedel shears

Area B: N = 1643
Area C: N = 1591
Area D: N = 1479
Area E: N = 1579
Area F: N = 1529
Area G: N = 1703

Area A: N = 1066
Area H: N = 1404

A	B	C	D	E	F	G	H
E1 = 0.5160 E2 = 0.4783	E1 = 0.5669 E2 = 0.4330	E1 = 0.5414 E2 = 0.4585	E1 = 0.5288 E2 = 0.4711	E1 = 0.5577 E2 = 0.4422	E1 = 0.5540 E2 = 0.4459	E1 = 0.5572 E2 = 0.4427	E1 = 0.5711 E2 = 0.4288
I	J	K	L	M	N	O	P
E1 = 0.5268 E2 = 0.4731	E1 = 0.5523 E2 = 0.4476	E1 = 0.5624 E2 = 0.4375	E1 = 0.5714 E2 = 0.4285	E1 = 0.5597 E2 = 0.4402	E1 = 0.5561 E2 = 0.4438	E1 = 0.5735 E2 = 0.4264	E1 = 0.6130 E2 = 0.3869

scale = 10 mm

Sample C4M

orientation 122 degrees

way up

Area P: N = 1606

Area I: N = 1482

Area J: N = 1852
Area K: N = 1936
Area L: N = 1899
Area M: N = 1836
Area N: N = 1494
Area O: N = 1836

Legend (left side):

- S1 clast microfabric
- S2 clast microfabric
- S3 clast microfabric
- S4 clast microfabric
- S5 clast microfabric

- subhorizontal Y-type Riedel shear
- moderately down-ce dipping R-type shears
- steeply down-ce dipping R'-type shears
- subvertical anastomosing dewatering foliation
- micritic carbonate cement

- sense of shear
- orientation of clast long axis
- alignment of clast long axes
- clay lined fractures, voids and pore spaces

orientation 122 degrees

way up

scale = 10 mm

Sample C6M

orientation 122 degrees

subhorizontal foliation (S2) defining Y-type Riedel shears

moderately inclined, up-ice dipping foliation (S3) forming dominant fabric

sinistral (down-ice) shear sense defined by asymmetrical microfabric

early foliation (S1) deformed by small-scale crenulations

subvertical anastomosing foliation (S5)

scale = 10 mm

Sample C6M

anastomosing zones of subvertical clast microfabric (S5)

moderately inclined down-ice dipping foliation (S4) defining extensional Riedel shears

down-ice dipping R-type Riedel shears

way up

Rose diagrams (top row):

- Area B: N = 1934
- Area C: N = 1501
- Area D: N = 1736
- Area E: N = 1740
- Area F: N = 1562
- Area G: N = 1632

Rose diagrams (left column):

- Area A: N = 1590
- Area I: N = 1046
- Area J: N = 1299

Rose diagrams (right column):

- Area H: N = 1297
- Area P: N = 1078

Rose diagrams (bottom row):

- Area K: N = 1725
- Area L: N = 1706
- Area M: N = 1526
- Area N: N = 1429
- Area O: N = 1616

Grid panels:

A	B	C	D	E	F	G	H
E1 = 0.5732	E1 = 0.5567	E1 = 0.5344	E1 = 0.5713	E1 = 0.5687	E1 = 0.5517	E1 = 0.5681	E1 = 0.5821
E2 = 0.4267	E2 = 0.4432	E2 = 0.4655	E2 = 0.4286	E2 = 0.4312	E2 = 0.4484	E2 = 0.4318	E2 = 0.4179

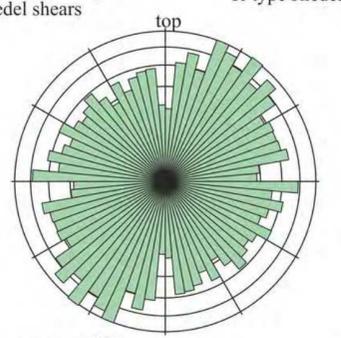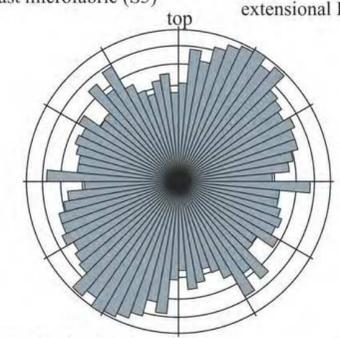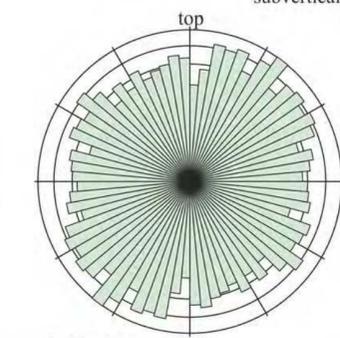| I	J	K	L	M	N	O	P
E1 = 0.5568	E1 = 0.5664	E1 = 0.5618	E1 = 0.5693	E1 = 0.5421	E1 = 0.5358	E1 = 0.5300	E1 = 0.5703
E2 = 0.4431	E2 = 0.4335	E2 = 0.4381	E2 = 0.4306	E2 = 0.4578	E2 = 0.4641	E2 = 0.4699	E2 = 0.4296

scale = 10 mm

Sample C6M

orientation 122 degrees

way up

sample X1M

sample Y1M

sample Z1M

Ice Flow Direction

Large horizontal displacement fabric

Down-ice dipping R Shear fabric

Microfabric anastomosing around rigid clast body

Superimposing subvertical microfabric

Dominant up-ice microfabric

Rotational turbate structures

10 Millimetres

Sub-Vertical Microfabric
Sub-Horizontal Microfabric
Down-Ice Dipping Microfabric
Up-Ice Inclined Microfabric
Horizontal 'Y' Riedel Shear
Down-Ice 'R/R' Riedel Shear
Clast
Turbate Microstructure
Sense of Shear

Ice Flow Direction

Down-ice dipping R shear fabric

Superimposing subvertical microfabric

Anastomosing fabrics around rigid body

Dominant up-ice microfabric

Rotational turbate structures

Large horizontal displacement fabric

10 Millimetres

Sub-Vertical Microfabric
Sub-Horizontal Microfabric
Down-Ice Dipping Microfabric
Up-Ice Inclined Microfabric
Horizontal 'Y' Riedel Shear
Down-Ice 'R/R' Riedel Shear
Clast
Turbate Microstructure
Sense of Shear

Ice Flow Direction

Superimposing subvertical microfabrics

Dominant up-ice microfabric

Down-ice dipping R Shear fabrics

Rotational turbate structures

Horizontal displacement fabric & shear

Void formed during thin-section dehydration

10 Millimetres

Sub-Vertical Microfabric
Sub-Horizontal Microfabric
Down-Ice Dipping Microfabric
Up-Ice Inclined Microfabric
Horizontal 'Y' Riedel Shear
Down-Ice 'R/R' Riedel Shear
Clast
Turbate Microstructure
Sense of Shear

Ice Flow Direction

S2

10 Millimetres   Way Up

Microlithon (No Fabric)
Clast Alignment
Microfabric
Strong Microfabric
Intense Microfabric

Ice Flow Direction

S3

10 Millimetres   Way Up

Microlithon (No Fabric)
Clast Alignment
Microfabric
Strong Microfabric
Intense Microfabric

Ice Flow Direction

S4

10 Millimetres   Way Up

Microlithon (No Fabric)
Clast Alignment
Microfabric
Strong Microfabric
Intense Microfabric

Ice Flow Direction

S5

10 Millimetres   Way Up

Sample: C5M

Sample: C6M

Sample: C6M

Sample: C1M

Sample: C2M
all photomicrographs taken in plane polarised light

Sample: C2M
scale bar = 1 mm

ice movement direction

(a)

base of overriding ice

ice

Y shear

down-ice dipping
R-type Riedel shears

up-ice dipping
P-type Riedel shears

dominant up-ice dipping
clast microfabric

subhorizontal Y-type
Riedel shears

Y shear

deforming sediment

asymmetrical (S-shaped) fabrics
defining sense of shear

(b) **Microstructural map of clast microfabrics**

clast microfabric domains
defined by shape-aligned
detrital grains

down-ce dipping
R-type shears

up-ice dipping clast
microfabrics
(dominant fabric)

subhorizontal
Y-type shears

subhorizontal clast
microfabric

10 mm

asymmetrical (S-shaped) fabrics defining sense of shear

down-ice dipping clast microfabric

different generations of clast microfabrics   sense of shear

subhorizontal Y-type Riedel shears   down-ice dipping R-type Riedel shears   steeply down-ice dipping R-type shears

a Sample C1 — subhorizontal fabric (S2) — (N = 15873)
b Sample C2 — subhorizontal fabric (S2) — (N = 17924)
c Sample C3 — subhorizontal fabric (S2) — (N = 21222)
d Sample C4 — subhorizontal fabric (S2) — (N = 20735)
e Sample C5 — subhorizontal fabric (S2) — (N = 25031)
f Sample C6 — subhorizontal fabric (S2) — (N = 23329)

Number of grains

down-ice dipping fabric (S4) — up-ice dipping fabric (S3)

— grain size < 0.25 mm
— grain size 0.25-0.5 mm
— grain size > 0.5 mm
— total clasts

— moving average (7 per.) < 0.25 mm
— moving average (7 per.) 0.25-0.5 mm
— moving average (7 per.) > 0.5 mm
— moving average (7 per.) total clasts

Sample C1

Top

All data (N = 15873)   Grain size < 0.25 μm (N = 8675)   Grain size 0.25-0.5 μm (N = 6270)   Grain size > 0.5 μm (N = 928)

Sample C2

Top

All data (N = 17924)   Grain size < 0.25 μm (N = 10879)   Grain size 0.25-0.5 μm (N = 6147)   Grain size > 0.5 μm (N = 898)

Sample C3

Top

All data (N = 21222)   Grain size < 0.25 μm (N = 13678)   Grain size 0.25-0.5 μm (N = 6516)   Grain size > 0.5 μm (N = 1030)

Sample C4

Top

All data (N = 20735)   Grain size < 0.25 μm (N = 13147)   Grain size 0.25-0.5 μm (N = 6596)   Grain size > 0.5 μm (N = 992)

Sample C5

Top

All data (N = 25031)   Grain size < 0.25 μm (N = 17190)   Grain size 0.25-0.5 μm (N = 6893)   Grain size > 0.5 μm (N = 948)

Sample C6

Top

All data (N = 23329)   Grain size < 0.25 μm (N = 15621)   Grain size 0.25-0.5 μm (N = 6799)   Grain size > 0.5 μm (N = 909)

orientation 122 degrees

ranges in E1 values

0.680
0.670
0.660
0.650
0.640
0.630
0.620
0.610
0.600
0.590
0.580
0.570
0.560
0.550
0.540
0.530
0.520
0.510

way up

scale = 10 mm

Sample C1M

way up

scale = 10 mm

Sample C2M

way up

scale = 10 mm

Sample C3M

way up

scale = 10 mm

Sample C4M

way up

scale = 10 mm

Sample C5M

way up

scale = 10 mm

Sample C6M

a

E1 eigenvalue

0.52 0.54 0.56 0.58 0.60 0.62 0.64 0.66

depth below base of soil layer (cm)

0 — 50 — 100 — 150 — 200

sample number

C1M
C2M
C3M
C4M
C5M
C6M

variation in average E1 value

zone of relatively more intense fabric development

decreasing average E1 value

b

E1 eigenvalue

0.80
0.75
0.70
0.65
0.60
0.55
0.50

shear strain curve for the gravelly Batestown till
from Thomason & Iverson (2006)

shear strain curve for sand-rich Douglas till
from Thomason & Iverson (2006)

range of average E1 eigenvalues
for the Polish tills

shear strain

0   20   40   60   80   100   120

direction of movement of ice

orientation 122 degrees

sense of shear imposed by the overriding ice

dip of main clast microfabrics

decrease in the relative intensity of S5

increase in the relative intensity of S3

zone of relatively more intense S5

increase in the relative intensity of S5

variable overprinting of S1 to S4 by the later S5 foliation

increased preservation of early S1 fabric

increase in the relative intensity of S2

increasing carbonate cementation/replacement of the matrix

Sample C1M

early foliation (S1) deformed by small-scale crenulations

moderately inclined, up-ice dipping foliation (S3) forming dominant fabric

subhorizontal to gently inclined foliation (S2)

S4

Sample C2M

S2

moderately inclined down-ice dipping foliation (S4)

S3

Sample C3M

S5

subvertical to very steeply dipping foliation (S5)

anastomosing foliation (S5) developed in finer grained matrix

Sample C4M

S2

Sample C5M

clast microfabrics defined by irregular domains

S3

Sample C6M

cross-cutting relationships between microfabrics allow the relative ages of the fabrics to be established

way up

S4

scale = 10 mm

Sample C1M

down-ice dipping R-type Riedel shears

steeply inclined down-ice dipping R'-type Riedel shears

subhorizontal Y-type Riedel shears

Sample C2M

asymmetrical microfabrics recording a sinistral sense of shear

Sample C3M

anastomosing fluid pathways associated with migration of meltwater through the diamicton (dewatering)

down-ice dipping R-type Riedel shears

Sample C4M

sinistral sense of shear recorded by Riedel shears consistent with ice movement direction

irregular patches of micritic carbonate cement

Sample C5M

distribution of carbonate replacement/ cementation appears spatially associated with S5 dewatering fabric

Sample C6M

way up

scale = 10 mm

S3 S4 S2 — Sample C1M

S3 S4 S2 — Sample C2M

S3 S4 S2 — Sample C3M

S3 S4 S2 — Sample C4M

S3 S4 S2 — Sample C5M

S3 S4 S2 — Sample C6M

Legend:
- S1 clast microfabric
- S2 clast microfabric
- S3 clast microfabric
- S4 clast microfabric
- S5 clast microfabric
- micritic carbonate cement
- areas of well-developed S5
- subhorizontal Y-type Riedel shears (S2)
- moderately down-ce dipping R-type shears (S3)
- sense of shear
- subhorizontal S2 fabric
- down-ice dipping S3 fabric
- up-ice dipping S4 fabric
- orientation of main fabrics
- fluid pathways

a

sense of sliding/displacement of grains past each other

grain sliding within the plane of evolving clast microfabric

progressive rotation of grain

grain rotation into plane of evolving clast microfabric

plane of evolving clast microfabric

b

low strain areas

larger clastic grains set in a finer grained matrix

larger grains influencing the partitioning of deformation into anastomosing higher strain zones

anastomosing higher strain zones which form the focus for clast microfabric development

partitioning of deformation within the matrix due to the presence of large clasts

c

down-ice dipping clast microfabric

areas with poorly aligned clasts

up-ice dipping clast microfabric

wrapping of clast microfabric around larger grains

microfabric domains

larger grains

partitioning of deformation within the matrix due to the presence of large clasts

a

ice

subglacial shear zone

till

pervasive shearing

cumulative strain
min — max

depth

bedrock or preexisting sediments

idealised cumulative strain curve

b

deformation partitioning

cumulative strain
min — max

depth

idealised cumulative strain curve

detachments dveloped at a deeper level within the subglacial shear zone

c

accretion of till in thin deforming layer at top of bed

cumulative strain
min — max

depth

massive till

idealised cumulative strain curve

accretion of well-mixed till layer at top of bed

subglacial deformation confined to active layer at top of the bed

shear imposed on underlying till overriding ice, size of arrow reflects changing magnitude of the cumulative strain imposed on the till within the active layer due to changes in the degree of ice-bed coupling